THE ASTROPHYSICAL JOURNAL, 422:486–507, 1994 February 20

THE SPATIAL STRUCTURE OF THE M87 GLOBULAR CLUSTER SYSTEM

DEAN E. MCLAUGHLIN AND WILLIAM E. HARRIS
Department of Physics and Astronomy, McMaster University, Hamilton, Ontario, Canada L8S 4M1
AND
DAVID A. HANES[1]
Department of Physics, Queen's University, Kingston, Ontario, Canada K7L 3N6
Received 1993 June 16; accepted 1993 August 19

ABSTRACT

Wide-field ($\sim 14' \times 14'$) CCD photometry in V of a field centered on M87 = NGC 4486 is used to examine the spatial structure, luminosity function, and specific frequency of the galaxy's globular cluster system (GCS). The salient results are as follows: (1) As recently reported by McLaughlin et al., the radial profile of the GCS shows an excess component which coincides in position and size with the cD envelope of the galaxy's halo. (2) In projection, the GCS of M87 is definitely elliptical in shape, with a major axis position angle which roughly coincides with that of the galaxy isophotes. However, its ellipticity increases with galactocentric radius faster than does the ellipticity of the underlying halo light. (3) The luminosity function of the GCS is well described by a Gaussian of dispersion $\sigma = 1.73$, and peak magnitude $V^0 = 24.2$. We confirm earlier claims that the bright half of the luminosity function shows no significant variation with galactocentric radius, out to $R \simeq 6'.8$. (4) We have computed the run of the ratio of globular cluster numbers to halo luminosity (specific frequency) over the region $1'.2 \lesssim R \lesssim 9'.1$; we find that the net specific frequency of M87, for $(m - M)_V(\text{Virgo}) = 31.0 \pm 0.2$, is $S_N = 14 \pm 4$, which is almost three times greater than for other, more normal Virgo ellipticals. A brief discussion of this high-S_N phenomenon is given, and we expand on the conclusion of McLaughlin et al. that the high S_N of the M87 cD envelope implies that this structure was accreted while still gaseous.

Subject headings: galaxies: elliptical and lenticular, cD — galaxies: individual (M87) — globular clusters: general

1. INTRODUCTION

Concentrations of globular clusters are found around nearly every major galaxy. The remarkable similarity of their first-order characteristics from one galaxy to another offers a unique opportunity to learn about both the earliest periods of star formation and the present-day structure in the halos of galaxies of all types and sizes (see Harris 1991 for a review of the collective properties of the globular cluster systems [GCSs] studied to date). The giant elliptical galaxies of the nearby, rich Virgo cluster have been of particular importance in establishing a fiducial picture of GCSs against which theoretical ideas and observations of other systems can be compared; and of these galaxies, the centrally located supergiant (and incipient cD) M87 (=NGC 4486) is perhaps the best studied. In this paper we use new wide-field CCD imagery to discuss three aspects of the M87 GCS: the spatial structure (both radial and azimuthal), the luminosity function, and the total population or specific frequency.

Baum (1955) first mentioned the presence of a large number of clusters around M87, and the distributon and colors of ~ 1000 of these objects were first investigated by Racine (1968a, b); deeper photometry was later carried out by Hanes (1971, 1977a, b). The first large-scale study of the spatial structure of the M87 GCS came from photographic star counts by Harris & Smith (1976). These data, and their subsequent reexamination (Harris & Racine 1979; Harris 1986), led to the major conclusion that the GCS of M87 is significantly less centrally concentrated than the galaxy's stellar halo light. This same result has now been found in many other giant elliptical systems (see Harris 1986, 1991). Soon after, Strom et al. (1981) and Forte, Strom, & Strom (1981) found that the globulars in M87 and the other Virgo ellipticals are everywhere bluer than the halo light and become systematically bluer (and, by assumption, more metal-poor) with galactocentric radius. These metallicity data, together with the shallowness of the GCS projected radial profile, suggest that globular clusters might be older than the rest of the halo population, and perhaps were the first tracers of galactic halos to appear during galaxy formation.

With the advent of CCD photometry, several new programs, beginning with those of van den Bergh, Pritchet, & Grillmair (1985) and Cohen (1988), were undertaken to observe the inner regions of the GCS in M87, and to obtain a deeper globular cluster luminosity function (GCLF). Of particular interest is the finding of Lauer & Kormendy (1986) and Grillmair, Pritchet, & van den Bergh (1986) that the GCS profile becomes even shallower inside a galactocentric radius of $R \simeq 1'.5$. Lauer & Kormendy deduced that the GCS has a core radius R_c which is an order of magnitude larger than that of the galaxy spheroid light. This behavior appears in the GCSs of many giant ellipticals (Harris et al. 1991). Recently we have found (McLaughlin, Harris, & Hanes 1993, hereafter MHH) that the large-scale radial distribution of the M87 GCS shows an excess of globulars from $R \simeq 4'.5$ outward, which is just where the stellar cD envelope begins (de Vaucouleurs & Nieto 1978). This discovery has implications for the formation processes of cD envelopes (MHH; and § 6.1 below). We look again at the radial distribution of the M87 GCS in § 3.

[1] Visiting Astronomer, Kitt Peak National Observatory, operated by the Association of Universities for Research in Astronomy, Inc., under contract with the National Science Foundation.

By contrast, the other aspect of the space distribution of the M87 GCS—the azimuthal distribution—has been largely neglected to data. Harris & Smith (1976), Grillmair et al. (1986), and Cohen (1988) were able to conclude only that the M87 GCS is significantly elliptical, and is oriented roughly in accord with the galaxy light. In § 4 we consider the angular distribution of the M87 globulars in more detail and derive for the first time a rough ellipticity profile for the GCS.

The GCLF (number of clusters per unit magnitude) was first quantified for M87 by Racine (1968a). Deeper and more comprehensive photographic photometry was carried out by Hanes (1977a, b), who fitted the GCLFs of M87 and several other Virgo ellipticals with Gaussian models and used them as standard candles to derive a Virgo distance measurement (Hanes 1977b). Since that time the use of GCLFs as distance indicators has been greatly refined as CCD imaging has permitted, much deeper photometry (see especially Hanes & Whittaker 1987; Harris et al. 1991; Secker & Harris 1993). In § 5 we discuss this point further and present the luminosity distribution of the globular clusters in our own sample, along with its implications for the Virgo distance modulus. We also address in § 5, the question of possible radial variations in the globular cluster luminosity function.

Another well-known feature of the M87 GCS, which was implicit in even the earliest data but was first quantified in the observations of Harris & Smith (1976) and Hanes (1977a), is that about three times as many globular clusters are found around M87 as is normal for the galaxy's luminosity; it is the prototypical "high specific frequency" system. This result has been verified numerous times (Harris & Racine 1979; Harris & van den Bergh 1981; Harris 1986; Grillmair et al. 1986; Cohen 1988), and similar overabundances have been found in the centrally dominant gE/cD galaxies of several other clusters (see Harris 1991 and Harris, Pritchet, & McClure 1993 for reviews). In § 6 we discuss our M87 data in this context, and the "high-S_N" phenomenon in general.

2. OBSERVATIONS AND REDUCTIONS

Our data are the same as described in an earlier paper (MHH). They were collected on the night of 1991 February 20 with the ST2K CCD at the prime focus of the 4 m telescope at KPNO. The field is 2012 × 2044 pixels in size at a scale of 0.″42 pixel^{-1}, thus ~14′ on a side. Three exposures were taken in the V band and then averaged to make the final image, with a total exposure time of 2400 s. The field is roughly centered on M87, giving complete areal coverage of the galaxy to a projected radius of 6.′7, and partial coverage out to $R \sim 9.'2$. Our main goal was to obtain information about the wide-field spatial structure of the GCS, so the innermost region of the frame ($R \lesssim 1.'05$) was allowed to become overexposed. Severe incompleteness of the counts in the annulus $1.'05 \leq R \leq 1.'21$ led us to reject that portion of the frame as well.

2.1. *Instrumental Magnitudes and Calibration*

We used the standard IRAF version of the PSF-fitting photometry package DAOPHOT (Stetson 1987) to reduce the data. Preliminary inspection of typical stellar profiles showed significant changes in the PSF structure across the frame. We divided the image into four large subrasters (allowing some overlap to intercompare the final photometry) and constructed separate PSFs for each, using ~10–15 moderately bright stars in each region. The reduction procedures described below were then applied uniformly to each subimage, and the final star lists were merged at the end. Figure 1 illustrates the way in which we divided the image. The PSF FWHM in the south region is 1.″24; in the west area, 1.″35; in the north, 1.″46; and the east region has a severely elliptical PSF with a FWHM of ~2″. On this basis (and because of significant incompleteness of the data in this region even at $V = 23$), the information from the east sector was ignored and is not discussed further.

Because DAOPHOT uses a local sky value in its estimation of the instrumental magnitudes, it is useful to remove any large-scale gradients in the background light distribution (in this case, the M87 halo light). To achieve this, we effectively subtracted the galaxy light by applying the iterative procedure outlined by Fischer et al. (1990). We used DAOFIND/PHOT to obtain an initial list of positions and aperture magnitudes to be used as input to ALLSTAR, which fitted the semiempirical PSF to them, and subtracted them from the frame. The residual image was then median-filtered to produce a heavily smoothed "galaxy," which was subtracted from the *original* frame. This sequence of operations was repeated four times, with filter apertures of successive widths 21, 15, 9, and 9 pixels. Then a final sequence of DAOFIND/PHOT/ALLSTAR was run twice, with a detection threshold of 3 σ. Any detections in a number of saturated or cosmetically defective regions of the frame were excised from the star lists, with the remaining magnitudes and positions being taken as final. The sky-flattened version of our frame is shown as Figure 1.

We compared the ALLSTAR photometry obtained within the three different areas of the image using the overlap regions (see Fig. 1) in order to normalize all the PSF-fitted magnitudes to the same zero point. The results of this comparison are presented in Figure 2. The means offsets (weighted by $1/\sigma^2$, the photometric error returned by ALLSTAR) are

$$\langle v_{\rm west} - v_{\rm south} \rangle = -0.069 \pm 0.041 \qquad (1a)$$

and

$$\langle v_{\rm north} - v_{\rm South} \rangle = -0.131 \pm 0.063\ , \qquad (1b)$$

where the west-south difference was calculated from 157 common *starlike* detections in the overlap zone (see § 2.3), and the north-south offset from 124 stellar objects in common. We added the appropriate corrections to the west and north magnitudes to reduce the entire data set to the internal magnitude scale for the south field.

Finally, same-night imaging of several standard stars was used to transform the instrumental (ALLSTAR) magnitudes to the true V scale. We selected 24 moderately bright and well-isolated stars throughout the south region and measured their magnitudes with PHOT, using the same large aperture as for the standard stars. Comparison with the PSF magnitudes then set the zero point of our V scale to within ±0.05 mag.

2.2. *Artificial Star Tests*

We used DAOPHOT's ADDSTAR routine and our empirical PSFs to add a total of ~15000 artificial stars (scaled PSFs) to the original image, uniformly distributed in magnitude and position, in groups of only a few hundred at a time so as not to change the character of the frame. We then repeated the reduction process and compared the retrieved stars to the added ones in each of several magnitude and radial bins, thus obtaining the (in)completeness of the data, as a function of magnitude and radius, and an estimate of the internal photometric error.

The completeness functions for our frame are presented in Tables 1–3; the fraction f is just the ratio of the number of

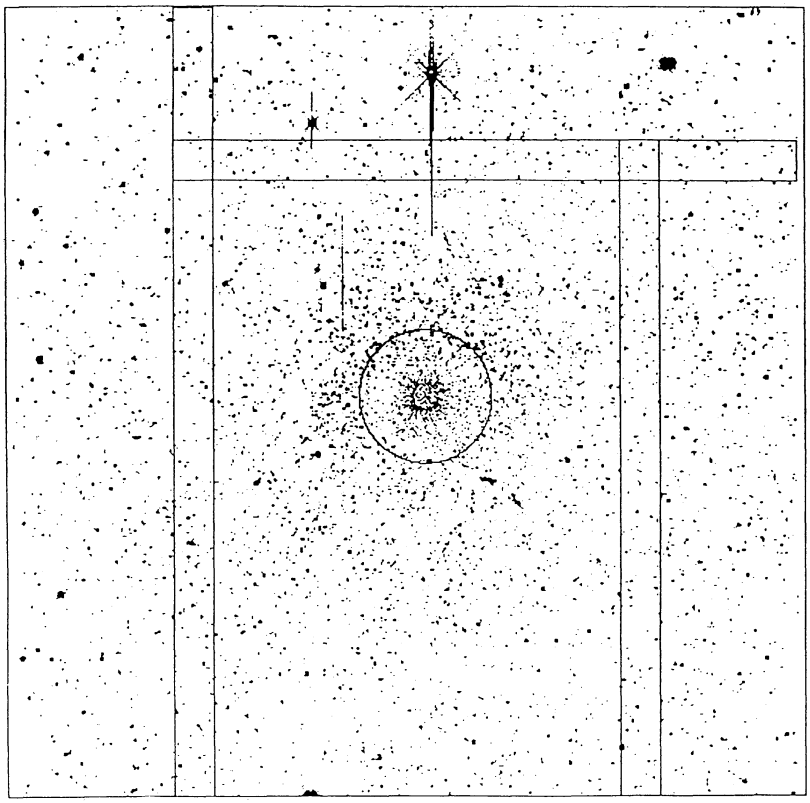

FIG. 1.—The galaxy-subtracted CCD image of the M87 GCS. North is at the top, and east is to the left. The circle has a radius of 1'.21 and borders the unusable area of the image. The division of the frame and the regions of overlap between the four subrasters are indicated. Our designations of north, south, east, and west for these four sections are self-explanatory.

artificial stars recovered by the reduction to the number added. Not surprisingly, f is different from one region to another. Also, there is a radial dependence within the south subraster, because of crowding and noise near the center of the galaxy; however, outside of $R \sim 3'$ there are no significant changes in f, and it is independent of position in the west and north regions as well.

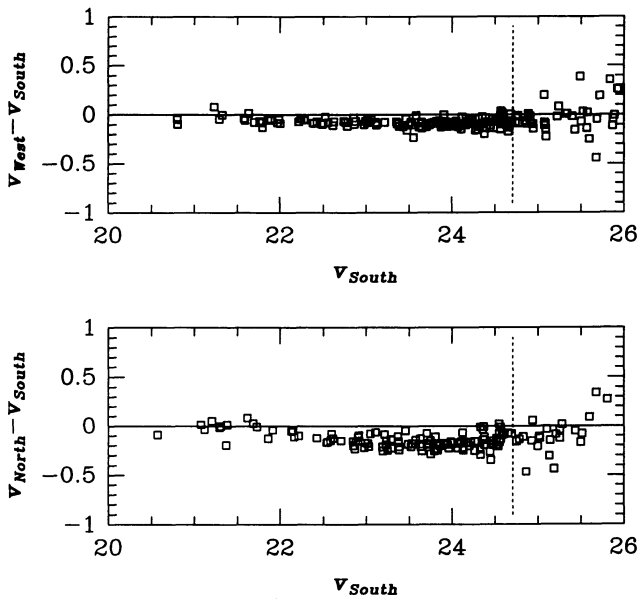

FIG. 2.—Comparison of the photometry obtained with the PSFs constructed from the south, west, and north regions of the frame. The magnitudes are instrumental, and the approximate limiting magnitude of $v_{south} \simeq 24.7$ ($V_{lim} = 24$) is marked.

In Figure 3 we display the completeness functions graphically; the south f (Fig. 3*a*) is the composite for the whole area. The error bars reflect the intrinsic binomial uncertainty of this quantity (Bolte 1989). Overlaid on the datapoints is an interpolation formula:

$$f = \frac{1}{2}\left[1 - \frac{\alpha(V - V_{lim})}{\sqrt{1 + \alpha^2(V - V_{lim})^2}}\right]. \quad (2)$$

This function (due to C. J. Pritchet) has been found to represent f accurately in a wide variety of conditions. In the limit of large α, it is just a step function which "turns off" at the limiting magnitude V_{lim}. The two free parameters (α and V_{lim}) are found by a simple maximum-likelihood routine; their values for each of our completeness functions are given in Table 4. Upon weighing all of this, we have adopted $V = 24$ as our limiting magnitude for the analysis that follows; no data fainter than this limit were used.

Finally, in Table 5 we present the results of a comparison between the artificial star magnitudes as recovered in the reduction process and the known input magnitudes. In the case of the south sector, the artificial stars added at *all radii* were considered.

2.3. *Image Classification*

We removed faint background galaxies (nonstellar images) from our star lists by using an automated image classification scheme which is described fully by Harris et al. (1991).

TABLE 1

SOUTH COMPLETENESS FUNCTIONS

	ANNULUS															
	$1'.21 \le R \le 1'.40$		$1'.40 \le R \le 1'.62$		$1'.62 \le R \le 1'.87$		$1'.87 \le R \le 2'.16$		$2'.16 \le R \le 2'.49$		$2'.49 \le R \le 2'.88$		$R \ge 2'.88$		$R \ge 1'.21$	
V[a]	N_{add}	f	N_{add}	f	N_{add}	f	N_{add}	f	N_{add}	f	N_{add}	f	N_{add}	f	N_{add}	f
20.00–20.25	2	1.000	3	1.000	4	1.000	11	1.000	6	1.000	10	1.000	137	0.978	173	0.983
20.25–20.50	5	1.000	15	1.000	20	1.000	26	1.000	29	1.000	26	1.000	169	1.000	290	1.000
20.50–20.75	6	1.000	22	1.000	18	1.000	24	1.000	35	1.000	45	0.978	129	0.992	279	0.993
20.75–21.00	9	1.000	13	1.000	21	0.952	29	1.000	30	1.000	49	0.980	161	1.000	312	0.994
21.00–21.25	9	1.000	20	1.000	26	1.000	34	1.000	25	1.000	49	1.000	140	1.000	303	1.000
21.25–21.50	3	1.000	21	0.952	19	0.947	24	0.958	37	0.974	42	1.000	145	1.000	292	0.987
21.50–21.75	10	1.000	11	1.000	19	1.000	23	1.000	33	1.000	41	1.000	148	1.000	285	1.000
21.75–22.00	5	1.000	13	1.000	15	1.000	26	0.962	27	0.963	47	1.000	153	1.000	286	0.993
22.00–22.25	17	1.000	45	0.978	55	1.000	80	1.000	91	0.989	132	0.992	317	0.991	737	0.989
22.25–22.50	32	1.000	45	0.978	56	0.982	71	0.972	101	1.000	124	1.000	349	0.989	778	0.990
22.50–22.75	30	1.000	43	0.953	51	0.961	76	0.934	100	0.980	119	0.992	344	0.985	763	0.972
22.75–23.00	29	0.897	35	0.914	61	0.885	81	0.951	79	0.962	102	0.980	333	0.973	720	0.955
23.00–23.25	25	0.800	39	0.846	48	0.938	83	0.904	102	0.912	154	0.942	344	0.956	795	0.927
23.25–23.50	38	0.842	34	0.882	52	0.827	91	0.857	110	0.845	123	0.878	313	0.911	761	0.870
23.50–23.75	28	0.464	34	0.676	47	0.596	67	0.716	101	0.792	133	0.782	316	0.788	726	0.742
23.75–24.00	27	0.519	41	0.390	51	0.412	89	0.483	103	0.592	127	0.551	344	0.669	782	0.570
24.00–24.25	30	0.267	38	0.342	47	0.298	76	0.237	110	0.309	133	0.346	313	0.332	747	0.315
24.25–24.50	1	0.000	5	0.000	3	0.333	11	0.091	13	0.077	16	0.188	118	0.169	167	0.154

[a] The data are everywhere 100% complete for $V < 20$.

This program takes the final ALLSTAR position and PSF magnitude for each detected image and computes a number of image moments which are then used to distinguish between stellar and nonstellar (extended or diffuse) objects. Two of these moments proved to be particularly useful in this context; they are

$$r_{-2} \equiv \left[\frac{\sum I/(r^2 + 0.5)}{\sum I}\right]^{-1/2} \tag{3a}$$

and

$$m_{ap} \equiv k - 2.5 \log \sum_{r=0}^{r=r_{max}} I_i , \tag{3b}$$

where I is the sky-subtracted intensity in a pixel at radius r

TABLE 2

WEST COMPLETENESS FUNCTION

V[a]	N_{add}	f
20.00–20.25	56	1.000
20.25–20.50	51	0.980
20.50–20.75	56	1.000
20.75–21.00	50	1.000
21.00–21.25	53	1.000
21.25–21.50	54	1.000
21.50–21.75	47	1.000
21.75–22.00	60	1.000
22.00–22.25	64	1.000
22.25–22.50	46	1.000
22.50–22.75	49	1.000
22.75–23.00	57	0.982
23.00–23.25	45	0.978
23.25–23.50	42	0.857
23.50–23.75	56	0.714
23.75–24.00	51	0.569
24.00–24.25	40	0.200
24.25–24.50	36	0.194

[a] The data are everywhere 100% complete for $V < 20$.

TABLE 3

NORTH COMPLETENESS FUNCTION

V[a]	N_{add}	f
20.00–20.25	42	1.000
20.25–20.50	46	1.000
20.50–20.75	32	1.000
20.75–21.00	51	1.000
21.00–21.25	41	0.976
21.25–21.50	52	1.000
21.50–21.75	55	0.982
21.75–22.00	52	1.000
22.00–22.25	42	1.000
22.25–22.50	41	0.976
22.50–22.75	58	0.948
22.75–23.00	43	0.953
23.00–23.25	61	0.885
23.25–23.50	55	0.800
23.50–23.75	41	0.585
23.75–24.00	48	0.354
24.00–24.25	59	0.186
24.25–24.50	51	0.000

[a] The data are everywhere 100% complete for $V < 20$.

TABLE 4

PARAMETERIZED COMPLETENESS FUNCTIONS

Zone	α	V_{lim}
South:		
(1'.21–1'.40)	1.81	23.78
(1'.40–1'.62)	1.79	23.82
(1'.62–1'.87)	1.84	23.82
(1'.87–2'.16)	2.12	23.85
(2'.16–2'.49)	2.18	23.93
(2'.49–2'.88)	2.26	23.95
($R \ge 2'.88$)	2.58	23.99
($R \ge 1'.21$)	2.17	23.93
West	2.83	23.88
North	2.38	23.70

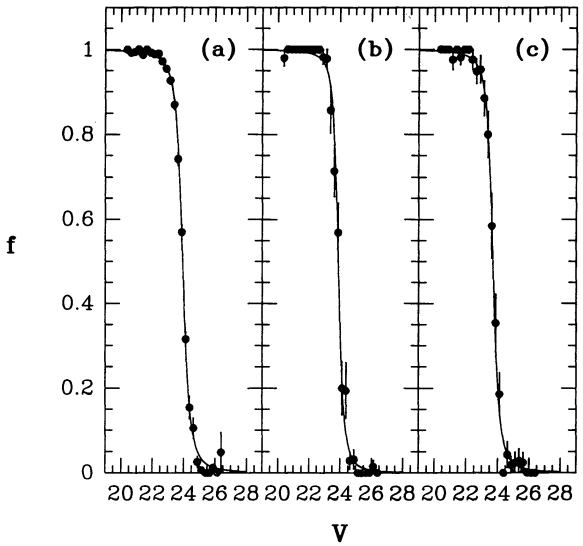

FIG. 3.—Completeness functions of the three subimages. (*a*) South region: $V_{lim} = 23.9$ (composite function; see text). (*b*) West area: $V_{lim} = 23.9$. (*c*) North sector: $V_{lim} = 23.7$. The solid curves in each case are the fits of eq. (2) (see Table 4).

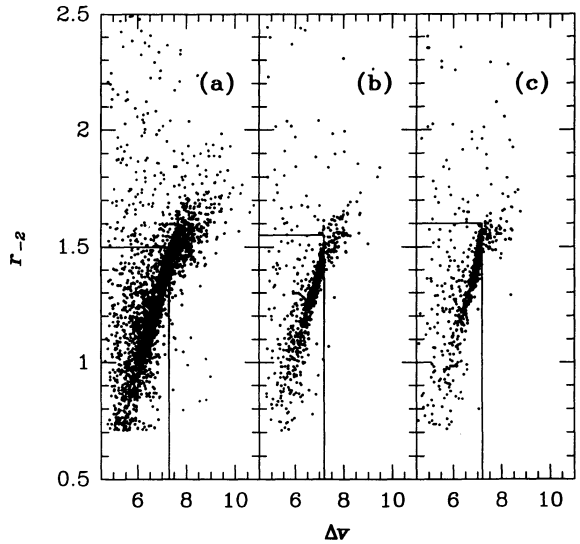

FIG. 4.—Classification of our detections. The borders of the boxes are for the south region (*a*), $r_{-2} \leq 1.50$ and $\Delta v \leq 7.3$, for the west area (*b*), $r_{-2} \leq 1.55$ and $\Delta v \leq 7.2$, and for the north (*c*), $r_{-2} \leq 1.60$ and $\Delta v \leq 7.2$. Objects falling outside these boxes are taken to be nonstellar.

(measured in pixels) from the centroid of the object (as determined by ALLSTAR), and the summations are taken over all pixels brighter than the detection threshold. The r_{-2} quantity is a discretized version of the corresponding Kron (1980) monent; it preferentially weights the central light of an image. The moment m_{ap} is clearly just an isophotal aperture magnitude. In our applications we fixed r_{max} to be 3 pixels and enabled the program to correct for crowding effects (according to the algorithm of Kron 1980) outside a 2 pixel radius.

In practice, we found it more convenient to use r_{-2} and the difference moment $\Delta v \equiv v_{psf} - m_{ap}$ to separate galaxies from "stars"; Δv should be smaller for stars than for galaxies, if the r_{max} used to find m_{ap} is close to the PSF FWHM. Figure 4 shows how our detections were distributed in the (Δv, r_{-2})-plane; in all three subimages, the "stellar" sequence is clearly defined from our artificial star experiments (Fig. 5). We culled from our star lists all those objects which fell outside the boxes drawn; the scatter off of the stellar sequence toward the upper left-hand corners of these boxes is an artifact of the photometric error at *faint* magnitudes.

Our choices of cutoff boundaries for r_{-2} and Δv resulted in a misclassification of ~2%–3% of the artificial stars as galaxies, for $19 \leq V \leq 24$ (even at the faintest magnitudes, that is, $23.5 \leq V \leq 24$, the fraction of wrongly rejected stars is only ~5%–6%); we made no attempt to correct for this effect. In all, ~16% of our real detections with $19 \leq V \leq 24$ were rejected as nonstellar, leaving us with a total of 3624 objects in this magnitude range.

TABLE 5

ARTIFICIAL STAR MAGNITUDE COMPARISONS

V (input)	SOUTH ⟨ΔV⟩[a]	SOUTH σ	WEST ⟨ΔV⟩[a]	WEST σ	NORTH ⟨ΔV⟩[a]	NORTH σ
20.00–20.25.....	−0.001	0.008	−0.001	0.006	−0.002	0.005
20.25–20.50.....	−0.001	0.010	−0.002	0.007	−0.002	0.008
20.50–20.75.....	−0.002	0.013	−0.001	0.009	−0.009	0.054
20.75–21.00.....	−0.004	0.023	0.000	0.011	−0.001	0.022
21.00–21.25.....	−0.003	0.032	0.000	0.014	0.000	0.015
21.25–21.50.....	−0.004	0.027	0.002	0.021	0.000	0.021
21.50–21.75.....	−0.008	0.037	−0.006	0.034	−0.003	0.027
21.75–22.00.....	−0.005	0.044	0.003	0.033	−0.002	0.029
22.00–22.25.....	−0.006	0.056	−0.003	0.045	0.010	0.037
22.25–22.50.....	−0.004	0.068	−0.003	0.047	−0.012	0.042
22.50–22.75.....	−0.011	0.069	0.002	0.064	−0.021	0.072
22.75–23.00.....	−0.012	0.090	−0.007	0.061	0.024	0.075
23.00–23.25.....	−0.012	0.111	−0.002	0.079	0.004	0.089
23.25–23.50.....	−0.022	0.135	0.004	0.099	0.031	0.101
23.50–23.75.....	−0.002	0.159	0.034	0.108	0.060	0.136
23.75–24.00.....	0.051	0.181	0.064	0.147	0.129	0.147
24.00–24.25.....	0.083	0.200	0.063	0.221	0.146	0.203
24.25–24.50.....	0.190	0.183	0.140	0.179	...[b]	...[b]

[a] $\Delta V = V_{in} - V_{out}$.

[b] No artificial stars were recovered in this bin.

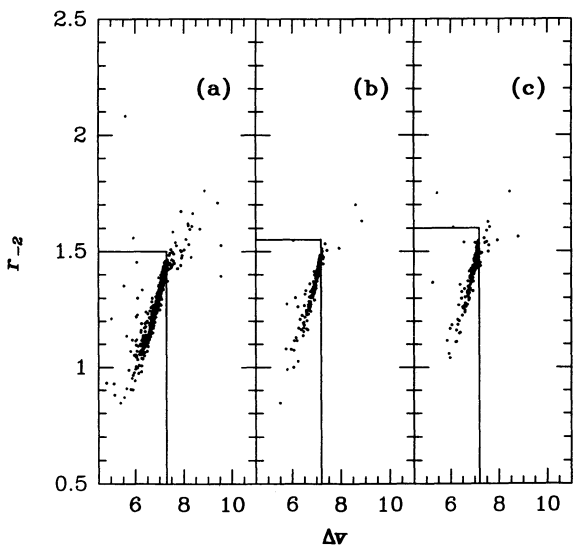

FIG. 5.—Same as Fig. 4, but for the artificial stars recovered in each subraster. For clarity, only ~1500 of the stars added to the south region (*a*) are shown.

In general, the neglect of any magnitude dependence in these classification criteria is an oversimplification. However, it is easy enough to determine the fraction g of misclassified artificial stars in each magnitude bin, and then to correct statistically the completeness function f by the multiplicative factor $(1 - g)$; the net effect is to *decrease* f at the faintest magnitude levels, and hence to *increase* the inferred true number of detections. In our case, though, such an effect was negligible (at the $\sim 5\%$ level); and in any event, only a modest fraction of detections were ultimately culled from our star lists. Further improvements could be made by using moments which measure image *shape* as well as sharpness (which is essentially what the r_{-2}, Δv moments examine). However, the only way to make genuinely major improvements in removing larger numbers background galaxies would be to acquire data taken in better seeing conditions (see Harris et al. 1991 for more extensive discussion).

Upon obtaining the final calibrated, culled, and merged star list (i.e., the composite of the north, west, and south subrasters), we divided the entire region $1'.21 \leq R \leq 9'.09$ into 14 concentric circular annuli (each of width $\log [R_2/R_1] = 1/16$); 12 sectors (each of angular width 30°, beginning with one centered on the projected semimajor axis of the galaxy isophotes); and twenty 0.25 magnitude bins between $V = 19$ and 24. The spatial binning is illustrated in Figure 6; the objects outside the largest drawn circle ($R = 9'.09$) were ignored. The counts in each three-dimensional bin were then divided by the appropriate completeness fraction, and their errors were estimated according to (Bolte 1989):

$$\sigma_N^2 \simeq \frac{N_{\rm obs}}{f^2} + \frac{(1-f)N_{\rm obs}^2}{N_{\rm add} f^3}, \quad (4)$$

where $N_{\rm obs}$ is the uncorrected count in a given bin and $N_{\rm add}$, f are given in Tables 1–3. After correction for incompleteness, we have a total population of ~ 4500 starlike objects with $19 \leq V \leq 24$ and $1'.21 \leq R$; given our estimate of the background surface density (§ 3), we can associate $\gtrsim 80\%$ of these with the globular cluster system of M87.

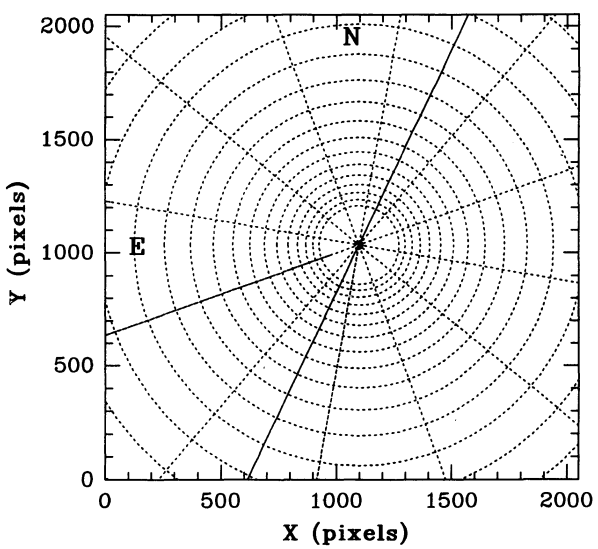

FIG. 6.—Radial and azimuthal bins used in constructing the spatial profiles of the GCS. The solid black line is the semimajor axis of the galaxy isophotes (155° E of N; Carter & Dixon 1978). The area to the left of $X = 450$ pixels is the east region, which has been ignored.

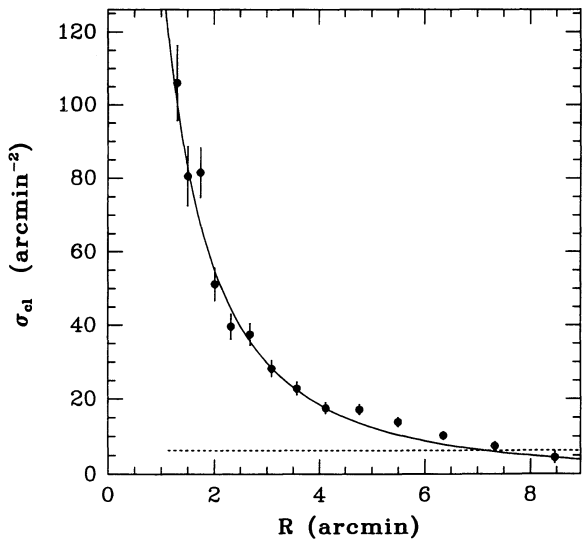

FIG. 7.—Background-subtracted, projected radial profile of the M87 GCS. Counts in each annulus include all starlike objects with $20 \leq V \leq 24$. The solid line is the best-fit $R^{1/4}$ law for the profile inside $R = 4'.5$ (eq. [6a] of the text); the excess (GCS envelope) at $R \gtrsim 4'.5$ is clearly visible. The dashed line is put at the background level of 6.3 arcmin^{-2}.

3. THE RADIAL DISTRIBUTION

In a previous paper (MHH) we reported the detection of a break in the radial profile of the M87 GCS at $R \simeq 4'.5$ and interpreted this structure as an echo of the cD phenomenon in the galaxy itself. Here we discuss some additional details of the radial density profile alluded to in that earlier work.

In Figure 7 the projected radial distribution of the M87 globulars is shown. The number counts in each ring are taken to represent the GCS density at the geometric mean radius of the annulus (Harris 1986); and the error bars reflect the counting errors as computed by equation (4) (this is the case for all the raw count errors in what follows). The dashed line is at our adopted background level of 6.3 ± 0.4 arcmin^{-2}; this value is determined by the method of Harris (1986), which gives the true background count as (nearly) the direct average of the value in the last radial bin and the asymptotic value of the best-fit de Vaucouleurs law for the *raw* surface density profile. However, the GCS of M87 is known to extend far beyond our limiting radius of $\sim 9'$, and Harris's method will overestimate the background density in such a situation; in fact, it is quite likely that our adopted background is artificially high by $\sim 25\%$ for just this reason. Such an overestimate will strongly affect only the outermost data points in our radial distribution, but works to strengthen our conclusions regarding the cD envelope (see MHH, and § 6 below).

In the representation of Figure 7, the morphological change in the region $4' \lesssim R \lesssim 5'$, which marks the beginning of the cD envelope of the halo light, can be seen as a brief plateau, followed by an apparently shallower falloff in the number density out to the limits of our field. This feature is independent of magnitude and direction (although once the data are divided into sectors and magnitude bins, the statistical significance of the feature is much diminished; undoubtedly, this is why it was not detected in earlier studies). We first consider the azimuthally averaged profile, as displayed in Figure 7, to param-

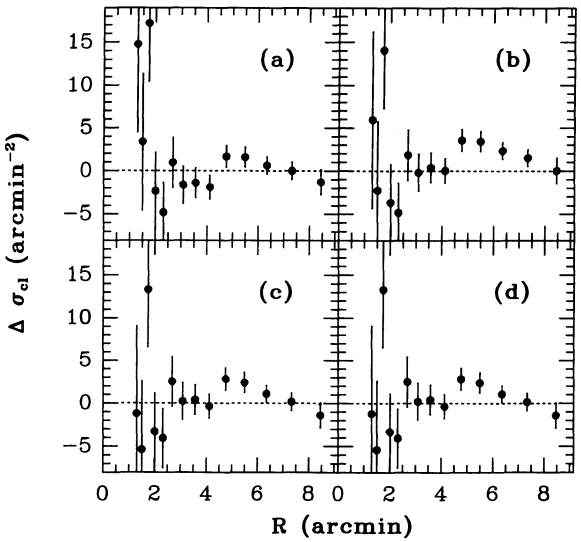

FIG. 8.—$(O-C)$ residuals of the fits (eqs. [5] and [6] in the text) to the GCS surface density profile. (*a*) Residuals of best-fit $R^{1/4}$ law for entire radial region. (*b*) $R^{1/4}$ law residuals for fit to $R \leq 4'.5$. (*c*) Power-law residuals for entire radial region. (*d*) Power-law residuals for $R \leq 4'.5$.

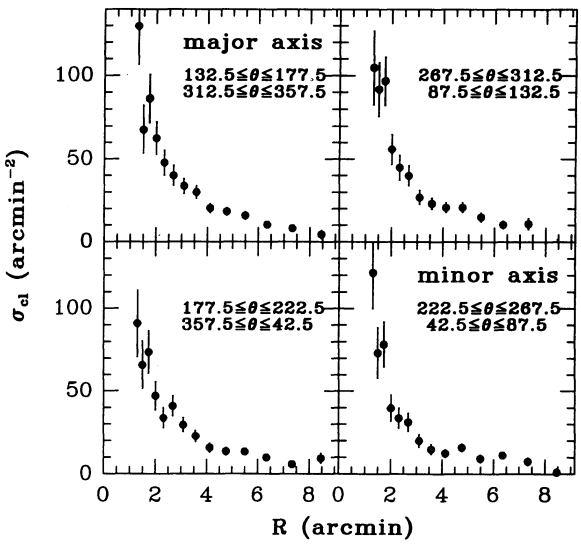

FIG. 9.—GCS radial profile in the four sectors (folded 45° wedges) of the frame. Angles are measured in degrees east of north.

eterize the overall distribution. The de Vaucouleurs law ($\sigma_{cl} = a_1 \times 10^{-a_2 R^{1/4}}$) and the scale-free power law ($\sigma_{cl} = kR^{-\alpha}$) were each considered, being fitted first to the entire profile, and then only to those points with $R \leq 4'.5$. The results of these fits are (for R in arcmin and σ_{cl} in arcmin^{-2}, and excluding the innermost and outermost points)

$$\log \sigma_{cl} = (3.97 \pm 0.11) - (1.88 \pm 0.08)R^{1/4}\,, \qquad (5a)$$

and

$$\log \sigma_{cl} = (2.18 \pm 0.03) - (1.47 \pm 0.06) \log R\,, \qquad (5b)$$

for the entire profile; and

$$\log \sigma_{cl} = (4.26 \pm 0.13) - (2.12 \pm 0.10)R^{1/4}\,, \qquad (6a)$$

$$\log \sigma_{cl} = (2.21 \pm 0.03) - (1.55 \pm 0.08) \log R\,, \qquad (6b)$$

for the GCS inside $R = 4'.5$. Figure 8 displays the $(O-C)$ residuals of these fits. The GCS envelope is most evident in the equation (6a) residuals (Fig. 8*b*), as a consistent excess of counts at $R \gtrsim 4'.5$. A similar jump, at the same radius, in the residuals of the other fits shows that this feature is also more or less model-independent.

To examine the possible dependence of this result on azimuth, we constructed radial profiles for each of eight sectors (of angular width 45°) about M87. The sectors were oriented so that two would be centered on the major axis of the galaxy isophotes (155°E of N; Carter & Dixon 1978, and Fig. 6), and two on the minor axis. The profiles in opposite sectors were then co-added, giving the four separate distributions displayed in Figure 9. Table 6 lists the parameters of the best-fit de Vaucouleurs and power laws in these sectors for $R \leq 4'.5$, and Figure 10 shows the deviations from the de Vaucouleurs fits. Figures 9 and 10 confirm that the identification of the cD envelope in the GCS counts is indeed a result of the large-number statistics afforded by our entire data set: the characteristic plateau and shallow falloff at $R \geq 4'.5$ are perhaps visible in each panel of Figure 9, as is the upward surge in the residuals of Figure 10, but the result loses statistical significance upon subdivision of the data. It might be argued that the envelope feature appears most prominent in the right-hand panels of Figures 9 and 10, and thus that it might be due to small-scale clustering (perhaps of background galaxies) somewhere in this half of our frame. However, we have inspected the radial distributions in the four individual sectors represented in these panels, and in the quadrants $42°.5 \leq \theta \leq 132°.5$ E of N

TABLE 6

GCS RADIAL PROFILE BY SECTOR

SECTOR[a] (E of N)	$R^{1/4}$ LAW[b]		POWER LAW[b]	
	$\log a_1$	a_2	$\log k$	α
$132°.5 \leq \theta \leq 177°.5$	3.93 ± 0.23	1.81 ± 0.18	2.17 ± 0.06	1.32 ± 0.13
$312.5 \leq \theta \leq 357.5$				
$177.5 \leq \theta \leq 222.5$	4.04 ± 0.26	1.96 ± 0.20	2.13 ± 0.06	1.43 ± 0.15
$357.5 \leq \theta \leq 42.5$				
$222.5 \leq \theta \leq 267.5$	4.74 ± 0.37	2.58 ± 0.23	2.23 ± 0.07	1.87 ± 0.17
$42.5 \leq \theta \leq 87.5$				
$267.5 \leq \theta \leq 312.5$	4.43 ± 0.27	2.22 ± 0.21	2.28 ± 0.06	1.62 ± 0.14
$87.5 \leq \theta \leq 132.5$				

[a] The major axis of the M87 halo light lies at 155° (335°) E of N, and the minor axis at 245° (65°) E of N.

[b] For objects with $20 \leq V \leq 24$; R in arcmin and σ_{cl} in arcmin^{-2}.

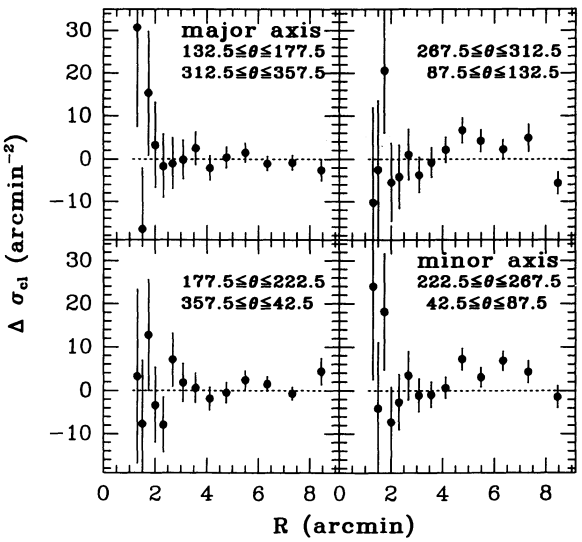

FIG. 10.—Residuals of the best-fit $R^{1/4}$ laws for the radial profiles of the four sectors of Fig. 9. The fits are made to the data inside $R = 4'.5$, and their parameters are given in Table 6.

and $222°.5 \leq \theta \leq 312°.5$ E of N, and find that the effect is still present in each of these profiles (in the sense that it is present in Figs. 9 and 10). Thus, the hump in the GCS radial profile is not grossly asymmetric, as it should be if it were caused by some clumping of objects in a small area of our frame. (We have not attempted to run more sophisticated statistical checks on the similarity of the profiles in the four sectors, such as the χ^2 or Kolmogorov-Smirnov tests, because the radially varying ellipticity of the GCS [§ 4] makes the profiles in the various directions intrinsically different.) Together with the close coincidence of the onset of this feature and that of the stellar cD envelope (MHH), we take this as evidence that the two effects are in fact different aspects of the same phenomenon.

Finally, we would like to establish that the existence of the hump is not dependent on magnitude. To show this, we use the χ^2 and Kolmogorov-Smirnov (KS) tests, with the weaker assumption that the slope of the radial profile of the GCS is a magnitude-independent quantity. We divide our counts into four 1 mag bins between $V = 20$ and 24 and compute a background surface density for each in the same way as before, yielding $\sigma_b(20 \leq V \leq 21) \approx 0$, $\sigma_b(21 \leq V \leq 22) \approx 0.4$ arcmin^{-2}, $\sigma_b(22 \leq V \leq 23) \approx 1.3$ armin^{-2}, and $\sigma_b(23 \leq V \leq 24) \approx 4.7$ arcmin^{-2}. Each of these estimates yields a background-subtracted radial profile with a slope between -1.8 and -1.9 in the $\log \sigma - R^{1/4}$ plane. An application of the standard two-sample KS test to any pair of profiles then shows that the hypothesis that they are drawn from the same parent population can be accepted at better than the 65% confidence level. A χ^2 test comparing the radial profiles in the four magnitude bins again shows a high level of agreement. Thus, we conclude that the GCS envelope is present at all magnitudes covered by our study.

4. THE AZIMUTHAL DISTRIBUTION

Previous analyses of the shape of the M87 GCS (Harris & Smith 1976; Grillmair et al. 1986; Cohen 1988) were able to show that the globulars roughly follow the galaxy light in terms of flattening and major axis position angle. While this is no surprise, neither is it a trivial result; for example, the GCSs of the S0 galaxy NGC 3115 (Hanes & Harris 1986a) and the Sa NGC 4594 (Harris, Harris, & Harris 1984; Bridges & Hanes 1992) are rounder than the spheroid isophotes, while the GCS of the E6 galaxy NGC 3377 may be even *flatter* than the halo light (Harris 1990). Such disagreement between galaxy isophotes and GCS isopleths may provide clues to the dynamical evolution of the GCS (e.g., Harris 1990).

The behavior of the GCS radial profile as outlined in the last section already tells us that the M87 GCS is elliptical, and that *its ellipticity increases with galactocentric radius R*, just as for the M87 halo light. To see this, we assume that the radial profile of the GCS along its semimajor axis (which need not coincide with the major axis of the galaxy isophotes) follows a power law, $\sigma_{cl} \sim a^{-\alpha}$; and along the minor axis, $\sigma_{cl} \sim (qa)^{-\beta}$, where q is just the axis ratio of the isopleth with semimajor axis a, and is in general a function of a (as usual, the ellipticity of an isopleth is given by $\epsilon = 1 - q$). Clearly, then, we have

$$\alpha = \beta\left(1 + \frac{\partial \ln q}{\partial \ln a}\right), \tag{7}$$

so that if the ellipticity *increases* with galactocentric distance, $\partial(\ln q)/\partial(\ln a) < 0$ and hence $\alpha < \beta$, that is, the GCS profile will follow a shallower exponent along its major axis than along its minor axis. (Note that the definition of the mean radius of an isopleth as $R \equiv (qa^2)^{1/2}$ then implies $\sigma_{cl} \sim R^{-2/(1/\alpha + 1/\beta)}$, so that the logarithmic slopes of the GCS profiles obtained from counts along the major axis [or in elliptical annuli], and from counts in circular annuli, will only agree if the flattening q is constant over the region of interest.)

We find that indeed $\alpha < \beta$ for the M87 GCS (for $R \leq 4'.5$; see Table 6). In fact, we have $\alpha/\beta = (1.32 \pm 0.13)/(1.87 \pm 0.17) = 0.71 \pm 0.13$, implying $q \sim a^{-0.29 \pm 0.13}$ for the M87 GCS in the region $1'.2 \lesssim R \lesssim 4'.5$; by comparison, the ellipticity profiles of Liller (1960), King (1978), Carter & Dixon (1978), and Cohen (1986) show a power-law relationship between q and a for the galaxy light with a negative slope of *at most* 0.12 in the same region. This indicates that at least parts of the GCS may be more flattened than the halo light, a point that we will return to below. In addition, the shallowest power-law exponent occurs for that portion of the GCS which lies in the sector centered on the galaxy's major axis (and the steepest slope is found around the galaxy's minor axis), suggesting that the GCS and the galaxy light share a common orientation to within $\sim 20°$.

Figure 11 also shows the behavior of the ellipticity of the GCS at large radii. Since the ratio of the surface density along the major axis to the minor axis density at a given *radius* is just $q^{-\alpha}$ (see below), the varying separation between the two sets of points in this plot suggests again that the shape of the GCS (i.e., q) changes with galactocentric distance. In particular, it is apparent that the GCS is rather round at small radii and becomes steadily flatter out to $R \simeq 4'.5$ (i.e., to the onset of the cD envelope), after which point it tends to become rounder once again. Interestingly enough, this last feature is *not* seen in the galaxy halo light (see Fig. 15) until (perhaps) $R \lesssim 7'$. If real, this contrast between halo and GCS is puzzling; but it should be kept in mind that only about half of the annulus $4'.43 \leq R \leq 6'.82$ lies on our frame (see below), so we cannot be sure that the relative roundness of the GCS in this outer region is representative of the mean distribution over the whole ring.

This preliminary evidence suggests that the *orientation* of the M87 GCS is more or less the same as that of the halo light, but

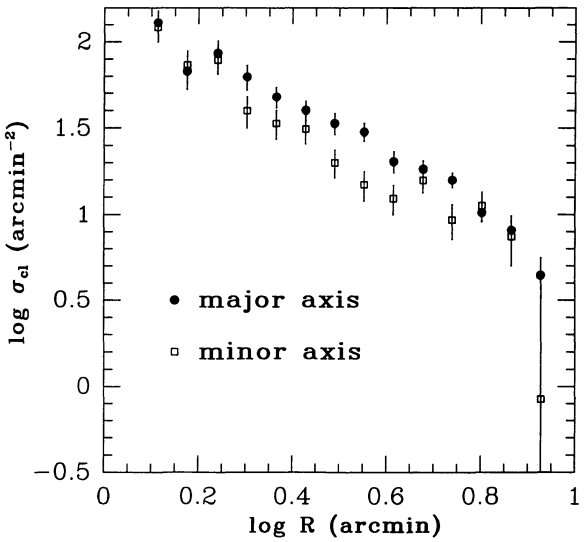

FIG. 11.—Comparison of the GCS profile in the 45° sectors centered on the semimajor and minor axes of the galaxy isophotes. The varying ellipticity of the GCS with radius is readily apparent.

that the *shapes* of the two systems may be in some ways significantly different. We now attempt to derive in more detail the ellipticity and position angle of the GCS at a number of different galactocentric radii. Two separate methods are used: moment analysis and maximum-likelihood profile fitting.

4.1. *The Method of Moments*

In analyzing the morphology of clusters of galaxies, Carter & Metcalfe (1980) employed the first five moments of the observed distribution to determine its ellipticity and major axis position angle; these moments are, as usual,

$$\mu_{10} = \langle x_i \rangle , \quad \mu_{01} = \langle y_i \rangle$$
$$\mu_{20} = \langle x_i^2 \rangle - \mu_{10}^2$$
$$\mu_{11} = \langle x_i y_i \rangle - \mu_{10}\mu_{01}$$
$$\mu_{02} = \langle y_i^2 \rangle - \mu_{01}^2 , \tag{8a}$$

where (x_i, y_i) is the location of an individual particle in the data set. The ellipticity and major axis position angle are then given by (see Trumpler & Weaver 1953 for a derivation)

$$\epsilon = 1 - \frac{\Lambda_-}{\Lambda_+}$$
$$\theta_p = \tan^{-1}\left(-\frac{\mu_{11}}{\mu_{02} - \Lambda_+^2}\right), \tag{8b}$$

with the semiprincipal axes of a given isopleth (major axis length Λ_+, minor axis length Λ_-) being given by (Buote & Canizares 1992)

$$\Lambda_\pm = \left[\frac{(\mu_{02} + \mu_{20}) \pm \sqrt{(\mu_{02} + \mu_{20})^2 - 4(\mu_{02}\mu_{20} - \mu_{11}^2)}}{2}\right]^{1/2} . \tag{8c}$$

(That is, $\Lambda_\pm^2$ are the eigenvalues of the moment of inertial tensor.)

Strictly speaking, we need to compute the moments (8a) from the distribution of globular clusters within a given annulus or aperture, but the identities (8b) hold only if this annulus has the same shape and orientation as the underlying distribution. Carter & Metcalfe (1980) therefore adopt an iterative procedure which successively adjusts the shape of the annulus (always keeping the mean radius $R \equiv (qa^2)^{1/2}$ constant) and recomputes the moments until the aperture and the distribution have the same shape. We have taken the same approach since it is relatively simple and eliminates the need to estimate the background surface density (the method applied to a uniform distribution of objects will simply return the shape of the annulus, so any need for iteration is due to the intrinsic shape of the GCS imposed on a uniform background, and convergence will return the shape and orientation of the GCS alone). One trivial modification we make is to adopt a centroid for the GC distribution and hold it fixed, at the center of the galaxy light on our frame ($X_0 = 1096$ pixels, $Y_0 = 1035$ pixels).

4.2. *A Maximum-Likelihood Approach*

Our second method is perhaps a more direct one. Again, we assume the GCS to show a power-law profile along its major axis, $\sigma_{cl} = ka^{-\alpha}$; then we can get at the projected shape of the distribution by considering the behavior of such a profile within the confines of *circular* annuli. The natural coordinate system here is one with the origin at the galaxy center, and with the x-axis lying along the semimajor axis of the GCS (which again may not be the major axis of the galaxy isophotes). Then using $x^2/a^2 + y^2/(qa)^2 = 1$ and $x = R\cos(\theta - \theta_p)$, $y = R\sin(\theta - \theta_p)$, we have

$$\sigma_{cl}(R, \theta) = kR^{-\alpha}[\cos^2(\theta - \theta_p) + q^{-2}\sin^2(\theta - \theta_p)]^{-\alpha/2} \equiv kR^{-\alpha}f(\theta) , \tag{9}$$

where θ_p is the position angle of the GCS semimajor axis relative to some reference axis and, as before, q is the axis ratio of the isopleth with major axis length a; R and θ fix the position of a given point and are measured out from the adopted galactic center and positive counterclockwise from the reference axis, respectively. Note that equation (9) tells us that $\sigma(R, \theta_p)/\sigma(R, \theta_p + \pi/2) = q^{-\alpha}$ (as mentioned above), where now q is the axis ratio of the isopleth with *minor* axis length R.

Evidently, if we take the average of the distribution (9) over $0 \le \theta \le 2\pi$ in a circular annulus of radius R and thickness dR, we recover the *radial* GCS surface density profile,

$$\sigma_{cl}(R) = \frac{1}{2\pi}kR^{-\alpha}\int_0^{2\pi} f(\theta)\,d\theta , \tag{10}$$

so that for constant q, $\sigma_{cl} \sim R^{-\alpha}$, as expected. Similarly, by averaging equation (9) over $R_1 \le R \le R_2$ in a wedge of position angle θ and width $d\theta$, the GCS azimuthal profile is obtained:

$$\sigma_{cl}(\theta) = \frac{2}{R_2^2 - R_1^2}\int_{R_1}^{R_2} kR^{-\alpha}f(\theta)R\,dR \equiv \sigma_0 f(\theta) , \tag{11a}$$

where

$$\sigma_0 = \frac{2k}{2-\alpha}\left(\frac{R_2^{2-\alpha} - R_1^{2-\alpha}}{R_2^2 - R_1^2}\right), \quad \alpha \ne 2$$
$$= 2k\left[\frac{\ln(R_2/R_1)}{R_2^2 - R_1^2}\right], \quad \alpha = 2 \tag{11b}$$

is the mean density along the semimajor axis ($\theta = \theta_p$) between

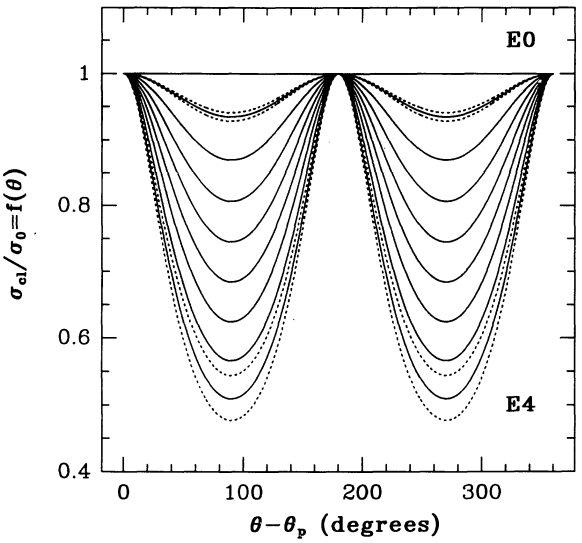

FIG. 12.—Theoretical normalized azimuthal surface density profile. θ_p is the position angle of the semimajor axis, and $\sigma_{cl}/\sigma_0 = [\cos^2(\theta - \theta_p) + q^{-2}\sin^2(\theta - \theta_p)]^{-\alpha/2}$, where α is the power-law slope of the GCS profile along its major axis. The solid lines are just this relation, with $\alpha = 1.32$, for values of the axis ratio q ranging from 1 (E0) to 0.6 (E4), in steps of 0.05. The broken lines indicate the effect of uncertainty in α: for a given ellipticity, the deeper curves have $\alpha = 1.45$, and the shallower profiles have $\alpha = 1.19$.

$R_1 \le a \le R_2$, if q is taken to be constant over this interval (recall that in general, q will have an intrinsic dependence on a, and hence on R and θ, so the integral in eq. [11a] cannot be evaluated without assuming some parametric representation of q as a function of a).

It is equation (11) which allows us to determine the flattening and orientation of the M87 GCS. Figure 12 shows the behavior of $f(\theta)$ for some typical axis ratios q; ideally, a comparison of these curves with the normalized surface density as a function of azimuthal angle (i.e., $\sigma_{cl}(\theta)/\sigma_0$) should allow us to determine the projected shape of the GCS. (It is assumed that k, α have been determined by fitting a power law to the major axis profile of the GCS in a certain magnitude interval.) To actually do this, we define a maximum-likelihood technique in which the probability for an object to be found in the intersection of the sector $(\theta, \theta + d\theta)$ with a given circular annulus is

$$p(\theta \mid q; \theta_p)\,d\theta = K\,\frac{f(\theta)\,d\theta}{\int_{\theta_1}^{\theta_2} f(\theta)\,d\theta} + (1 - K)\,\frac{d\theta}{\theta_2 - \theta_1}, \quad (12)$$

where $\theta_1 < \theta_2$ are the angles delimiting the intersection of our CCD frame and the annulus (e.g., for an annulus which lies entirely on the frame, $\theta_1 = 0$ and $\theta_2 = 2\pi$). In this formalism, $K \equiv N_{cl}/(N_{cl} + N_b)$ is the fraction of objects in the annulus which belong to the GCS; hence the second term in the definition of $p(\theta)$ is an attempt to account for the background contamination in our sample. We then compute the value of $p(\theta)$ for each object in the annulus and numerically search for those values of the parameters which maximize the joint probability distribution

$$P(q; \theta_p) \equiv \prod_{i=1}^{N_{cl}+N_b} p(\theta_i \mid q; \theta_p)\,. \quad (13)$$

4.3. *Results*

Each of the two procedures outlined above has advantages. The method of moments is preferable in the case where an accurate (or even reasonable) estimate of the background surface density is not available. It is also to be preferred if the photometric incompleteness is not a function of position in the frame, since objects as faint as the limiting magnitude can then be used in the calculation of the moments. However, if the incompleteness *does* have a radial dependence (as it does for us), only those data which are nearly 100% complete should be used. Also, the method requires that the annuli within which the moments are taken lie entirely in the frame. This is true only for $R \lesssim 4'.5$ in our case. Thus, we divided the area inside $R = 4'.5$ into three annuli ($1'.21 \le R \le 1'.87$; $1'.87 \le R \le 2'.88$; and $2'.88 \le R \le 4'.43$) and computed the ellipticity and major-axis position angle of the GCS within each (or, more accurately, within the elliptical annuli with $1'.21 \le (qa^2)^{1/2} \le 1'.87$, etc.).

On the other hand, our maximum-likelihood technique can be used even for those annuli which do not lie entirely on the frame (although clearly the results will in this case be strongly biased by any asymmetries in the distribution), but it does require an accurate knowledge of the background surface density and thus cannot be applied to data which suffer from significant photometric incompleteness. With this in mind, we applied this procedure to the same three annuli listed above, and to a fourth ($4'.43 \le R \le 6'.82$), which does not lie entirely on our frame, once the data from the east region are discarded as described in § 2.

The results from both these methods, applied only to those objects with $20 \le V \le 23$ for which photometric incompleteness is negligible, are presented in Table 7. The uncertainties associated with the ellipticity returned by the moments method have been calculated from an empirical formula given by Carter & Metcalfe (1980), which they obtained by applying their method to several synthetic galaxy clusters in a series of

TABLE 7

THE SHAPE OF THE M87 GCS

			MOMENTS		MAXIMUM LIKELIHOOD		ADOPTED	
ANNULUS	N[a]	AREA[b]	ϵ	θ_p[c]	ϵ	θ_p[c]	ϵ	θ_p[c]
$1'.21 \le R \le 1'.87$.....	229	4.75	...	...	$0.109^{+0.008}_{-0.012}$	75.4 ± 0.2	0.11 ± 0.01	75
$1'.87 \le R \le 2'.88$.....	342	14.84	0.227 ± 0.065	137.3 ± 8.0	$0.223^{+0.024}_{-0.021}$	143.1 ± 0.4	0.22 ± 0.02	140
$2'.88 \le R \le 4'.43$.....	499	35.36	0.306 ± 0.056	159.5 ± 5.0	$0.325^{+0.035}_{-0.032}$	162.9 ± 0.3	0.32 ± 0.03	161
$4'.43 \le R \le 6'.82$.....	423	48.77	...	...	$0.238^{+0.029}_{-0.022}$	146.0 ± 0.4	0.24 ± 0.03	146

[a] Total number of clusters and background objects with $20 \le V \le 23$.
[b] Units of arcmin^2; includes only those sectors used in the maximum-likelihood fitting.
[c] Measured in degrees east of north.

TABLE 8

THE AZIMUTHAL GCS SURFACE DENSITY PROFILE

SECTOR (E of N)	σ_{cl}[a]			
	$1'.21 \le R \le 1'.87$	$1'.87 \le R \le 2'.88$	$2'.88 \le R \le 4'.43$	$4'.43 \le R \le 6'.82$
$-10°$ to $+20°$	43.58 ± 9.53	25.50 ± 4.73	14.61 ± 2.45	(4.38 ± 1.10)
20–50	43.58 ± 9.44	14.40 ± 3.74	11.27 ± 2.15	(5.63 ± 1.15)
50–80	43.58 ± 9.36	19.90 ± 4.21	7.89 ± 1.86	...
80–110	53.02 ± 10.29	26.17 ± 4.84	9.11 ± 1.96	...
110–140	36.04 ± 8.54	18.13 ± 4.09	14.85 ± 2.41	...
140–170	(28.49 ± 7.70)	15.90 ± 3.82	16.88 ± 2.55	6.56 ± 1.16
170–200	(21.83 ± 6.92)	19.10 ± 4.15	15.53 ± 2.46	6.80 ± 1.18
200–230	(38.68 ± 8.97)	21.25 ± 4.39	11.52 ± 2.16	5.27 ± 1.08
230–260	47.36 ± 9.80	14.43 ± 3.66	10.16 ± 1.05	4.98 ± 1.06
260–290	53.02 ± 10.36	24.70 ± 4.66	11.14 ± 2.13	8.23 ± 1.28
290–320	53.02 ± 10.32	23.10 ± 4.50	12.49 ± 2.24	7.48 ± 1.22
320–350	43.58 ± 9.41	33.50 ± 5.36	13.50 ± 2.32	9.70 ± 1.35
σ_0	53 ± 7	24.7 ± 3.3	15.2 ± 1.7	8.1 ± 0.9

[a] For $20 \le V \le 23$, in units of arcmin^{-2}, corrected for $\sigma_b = 1.7 \pm 0.4$.

Monte Carlo simulations; the errors attached to the position angle are obtained similarly and were checked against results from a similar experiment done by McMillan, Kowalski, & Ulmer (1989). The uncertainties in this case depend both on the number of objects involved in the computation, and on the ellipticity returned by the method. The internal errors of the maximum-likelihood technique, on the other hand, have been estimated through the uncertainties in the slope of the GCS profile along the major axis ($\alpha = 1.32 \pm 0.13$), and in the background surface density, $\sigma_b(20 \le V \le 23) = 1.7 \pm 0.4$ arcmin^{-2} (§ 3). We estimate for our adopted parameters (which correspond to $\alpha = 1.32$), an uncertainty of *at best* $\pm 10\%$ in ϵ and $\pm 5°$–$10°$ in θ_p.

Table 8 and Figure 13 present the binned azimuthal profile of the M87 GCS in the four annuli listed above. In Figure 13 the adopted profiles from Table 7 are overlaid on the observed distributions. The value of σ_0 is determined from the *observed* profile (and not from eq. [11b]) once the position angle of the GCS is known (Table 7), by averaging the densities in the two sectors containing the semimajor axis. The reason for this is that equation (11b) is useful only when the observed distribution follows a power law almost exactly; any noise about the best fit will introduce a disagreement between the true and calculated values.

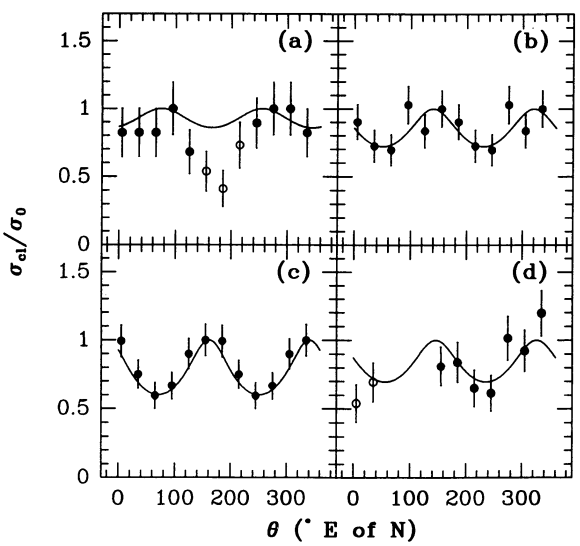

FIG. 13.—Azimuthal distribution of globular clusters in M87 with $20 \le V \le 23$, in four different circular annuli: (*a*) $1'.21 \le R \le 1'.87$, (*b*) $1'.87 \le R \le 2'.88$, (*c*) $2'.88 \le R \le 4'.43$, and (*d*) $4'.43 \le R \le 6'.82$. The data in panels (*b*) and (*c*) have been "folded," as mentioned in the text. The empty circles in (*a*) and (*d*) represent those sectors which were ignored in the estimation of the shape parameters ϵ, θ_p (see text). The solid curves delineate the adopted profile in each annulus, as listed in Table 7. χ^2 values for the fits are 0.45, 0.64, 0.34, and 0.94, for (*a*) to (*d*), respectively. The adopted values for σ_0 are given in Table 8.

We note here that the ellipticity returned by the method of moments for the innermost annulus was spuriously large (~ 0.3), owing to a noticeable patchiness in the distribution of objects there; many fewer bright objects than average are found in the quadrant $140 \lesssim \theta \lesssim 230°$ E of N. We therefore used only the maximum-likelihood estimation of the parameters for this annulus, and only the data outside of the offending quadrant. Interestingly, when the counts for $20 \le V \le 24$ in this annulus are corrected for incompleteness and binned (Fig. 14), the deficiency in this quadrant seems to disappear, and the data are well described by $\epsilon = 0.11$ and $\theta_p \simeq 105°$ E of N (notice that this is $\sim 30°$ away from the position angle quoted in Table 7; this points out the importance of having the annulus lie entirely on the frame). The values in parentheses in the second column of Table 8 (corresponding to the open circles in Fig. 13*a*) are in this quadrant.

Figures 13*b* and 13*c* show the best agreement between the computed and observed azimuthal profiles. This is undoubtedly because the two annuli involved here lie entirely on our frame and thus yield the most stable solutons for the shape parameters. In displaying these distributions, we have averaged the density in sectors 180° apart in order to match the "theoretical" profiles to the average of the observed profiles. The good agreement between the two illustrates that the maximum-likelihood technique, especially, finds its way through any noise to return a profile which accurately describes the *mean* distribution of the GCS in a given annulus.

Figure 13*d* shows the annulus $4'.43 \le R \le 6'.82$, which lies almost fully within the region of the cD envelope. The two empty circles (corresponding to the values in parentheses in col. 5 of Table 8) mark sectors which were not used in the maximum-likelihood solution for (ϵ, θ_p) because of the presence of bright, saturated stars, whose excision leaves a spur-

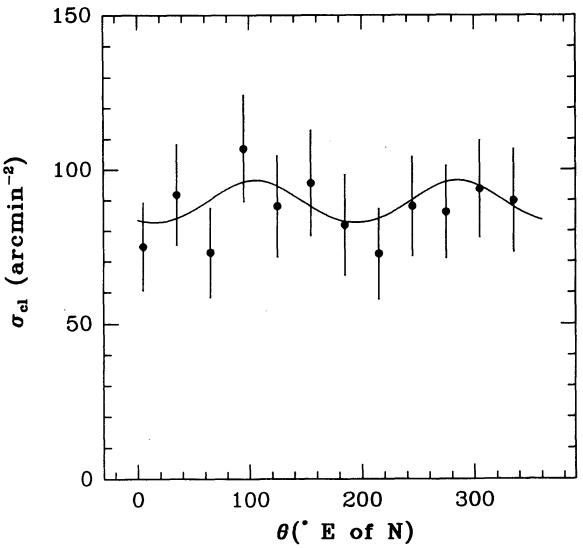

FIG. 14.—Reexamination of the azimuthal distribution of the GCS for $1'.21 \leq R \leq 1'.87$. This time those clusters with $20 \leq V \leq 24$ are represented. The curve has $\epsilon = 0.11$ ad $\theta_p = 105°$ E of N. In this case, $\sigma_0 = 96.5 \pm 11.5$ arcmin^{-2}, and the χ^2 statistic is 0.31.

iously low number of detected clusters in this region. Thus the shape parameters quoted for this annulus in Table 7 are much less secure than those for the two middle annuli. The sudden circularization of the GCS, apparent in Fig. 11, is reflected by the relatively lower ellipticity found for this annulus; but again, this may in turn reflect some systematic effect we are not aware of.

4.4. *Discussion*

In Figure 15, we compare the ellipticity profile of the M87 GCS, as derived above, to that of the galaxy's halo light. The adopted ellipticity of each annulus is plotted at the geometric mean radius of the ring. These results give for the GCS ellipticity profile a logarithmic slope of $\Delta \log q/\Delta \log a \simeq -0.27$ (for $R \leq 4'.5$), in good agreement with the value of -0.29 inferred above from the ratio of the major- and minor-axis

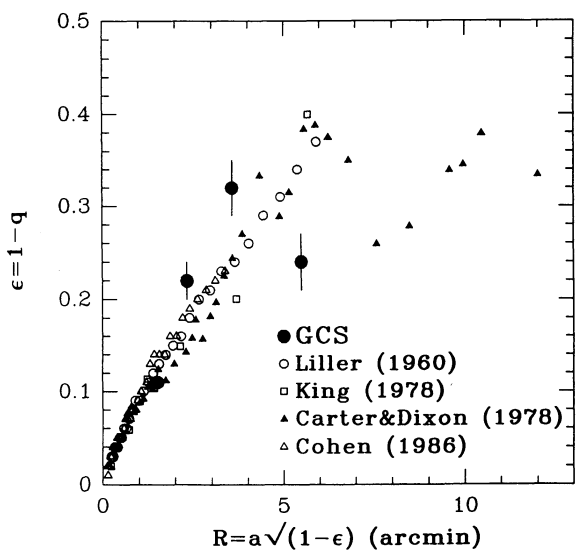

FIG. 15.—Comparison of the ellipticity profiles of the M87 GCS and halo light.

power-law slopes. We stress again that our most secure points are the middle two; the other annuli suffer from areal incompleteness such that the *position angle* of the innermost annulus and the *ellipticity* of the outermost annulus are particularly uncertain (and the position angle of our inner ring may be additionally suspect because of the small ellipticity there).

The data suggest that *the ellipticity gradient of the M87 GCS is steeper than that of the halo light*, at least inside $R = 4'.5$. This conclusion is strengthened when it is realized that we have probably overestimated the slope of the GCS density profile along its major axis and underestimated it along the minor axis: in order to arrive at α and β, we considered the radial distribution of the GCS in 45° wedges centered (roughly) on the principal axes; but σ_{cl} will be shallowest at $\theta = \theta_p$ exactly (and steepest at $\theta = \theta_p + \pi/2$), so α is steepened and β is made shallower by our binning method. The overestimate of α in particular means that our adopted ellipticities are underestimates of the true values. Indeed, for $\alpha = 1.19$ (even with a lower limit of $\sigma_b(20 \leq V \leq 23) = 1.3$ arcmin^{-2}), these ellipticities will move to the tops of the error bars in Figure 15. In summary, the M87 GCS has roughly the same projected shape as the halo light at $R \sim 1'$–$2'$, but is relatively flatter at larger radii.

An interpretation of this new result is not immediately obvious although two basic avenues seem open to us: either (1) the different slopes of the GCS and halo ellipticity profiles were imprinted on these systems at the time of galaxy formation, or (2) the two profiles started out being roughly similar in slope (perhaps with a constant, nonzero difference in ellipticity at all radii), but evolved differently. In the first case, it is perhaps relevant that dark matter halos are generally flatter than the visible parts of elliptical galaxies (e.g., Dubinski & Carlberg 1991). If the GCS is a relatively older and more extended population, it could be a better tracer of the DM potential at large radii, and might then be flatter than the stellar halo in these outer parts. The subsequent dissipative collapse of the gas which went on to form the bulk of the halo could then have led to its relatively rounder shape (Ryden 1992). Alternatively, a large part of the M87 GCS might have fomed in early (gaseous) mergers (e.g., Ashman & Zepf 1992) and thus may well have been given a different ellipticity gradient from the stars.

As far as the second scenario is concerned, one mechanism which might act to steepen the ellipticity gradient of the GCS over time is that proposed by Ostriker, Binney, & Saha (1989) to explain the large core radius of the GCS; if the globular clusters in M87 formed frequently on box orbits, then over a Hubble time the destructive effects of close encounters with the compact nucleus of M87 (which is perhaps a black hole of mass $\simeq 3 \times 10^9\ M_\odot$; Lauer et al. 1992 and references therein) could be felt out to distances of $\sim 1'$–$2'$; in particular, the removal of clusters on box orbits in these inner regions may well have left behind a relatively rounder GCS population. Therefore, even if the GCS initially had the same ellipticity gradient as the stellar halo (but was systematically flatter at all radii), the progressive circularization of the inner parts could have acted to produce the effect we see now. Quantitative modeling will be needed to see if this process alone can explain the size of the effect. In conjunction with this, it is interesting that the GCS of NGC 4594 (which also harbors a compact nucleus of mass $\sim 10^9\ M_\odot$; e.g., Kormendy 1988) has, like the M87 GCS, a large core radius, *and* is significantly rounder than the bulge light in the innermost regions (Harris et al. 1984; Bridges & Hanes 1992). The true cause of the GCS ellipticity gradient undoubtedly lies

somewhere between the purely initial and purely evolutionary scenarios we have suggested here.

Next we note the behavior of the orientation of the GCS over $1'.21 \leq R \leq 6'.82$. Given that the uncertainty in our GCS major-axis position-angle determinations is on the order of $\pm 10°$, and allowing for the much larger uncertainty in θ_p for our innermost annulus, we conclude that there is evidence neither for a *significant* GCS position-angle twist over these radii, nor for a significant deviation from the orientation of the M87 halo light (which also remain more or less constant at 155° E of N [Carter & Dixon 1978]; the three outer annuli have θ_p which are $\leq 15°$ away from this position).

Triaxility does not always produce position-angle twists in projected isopleths (and conversely, the presence of isopleth twists is not an unambiguous indication of triaxiality), so the negative (or, at best, marginal) detection of any axis twist here *does not* automatically imply that the M87 GCS is axisymmetric. Rather, it is possible for the intrinsic axis ratios of a triaxial figure to vary with radius in such a way that the projected ellipticity profile is seen to have a positive slope while the isopleths show no twisting (see, e.g., Franx, Illingworth, & de Zeeuw 1991); this may be what is occurring in both the stellar halo and the GCS of M87.

5. THE LUMINOSITY DISTRIBUTION

5.1. *The Globular Cluster Luminosity Function*

To first order, GCSs in galaxies of all morphological types and absolute luminosities exhibit a striking similarity in the relative numbers of clusters per unit magnitude (see e.g., Harris 1991). In particular, these globular cluster luminosity functions (GCLFs) are consistently well described by a Gaussian:

$$\phi(M_V) = A \exp\left[-\frac{(M_V - M_V^0)^2}{2\sigma^2} \right], \qquad (14)$$

with typical dispersions $\sigma \sim 1.0$–1.5, and means $-M_V^0 \sim 7.0$–7.5. The simplicity of this function, and its near-uniformity (specifically, the similarity of the peak luminosity M_V^0) from galaxy to galaxy, make the GCLF attractive as a standard candle; at the same time, its potential as a distance indicator makes it imperative to establish the precise form of the GCLF as firmly as possible. M87 especially, with its enormous population of globular clusters, holds great promise as a calibrator for the GCLF as a standard candle (at least for giant ellipticals). However, without data extending clearly deeper than the peak of the best-fitting curve, it is not possible to solve accurately for both σ and M_V^0 simultaneously (Hanes & Whittaker 1987; Secker & Harris 1993). The analyses of van den Bergh et al. (1985) and Cohen (1988) show the peak of the M87 GCLF to lie at $B^0 \simeq 25.0$, and the analyses of Harris et al. (1991) and Secker & Harris (1993) have shown rather conclusively that the peak of the GCLF for three Virgo gE's (NGC 4365, 4472, 4649) lies at $B^0 \simeq 24.5$–24.7. If we then adopt a mean color for the M87 GCS of $(B-V) \simeq 0.7$ (Couture, Harris, & Allwright 1990), we should expect to find $V^0 \gtrsim 24.0$, so that our data may just barely reach the turnover of the GCLF.

An additional complication in our case is the lack of a comparison background field, which is essential for a precise cleaning of the luminosity function to reflect the distribution of the globular clusters alone. Nevertheless, the size of our data set should allow a rather clear definition of the bright half of the luminosity function of the M87 GCS.

We present in Table 9 the derived GCLF $\phi(V)$ for M87. The second column lists the total number of starlike detections (both globulars and background/foreground objects) inside $R = 6'.82$ on our frame, after correcting for photometric incompleteness. The third column contains the luminosity function in our field at $R \geq 6'.82$; we have *defined* this region to be our background (but note that with $\sigma_b = 6.3$ armin^{-2}, we expect ~ 200 of these "background" detections to in fact be globular clusters), scaled it up by the ratio of the areas inside and outside $R = 6'.82$, and subtracted it from the raw LF (in col. 2) to obtain the residual GCLF, which is given in the last column. In Table 10 are listed the results of weighted nonlinear least-squares fits of a Gaussian to $\phi(V)$, assuming different values of the dispersion σ; a strong correlation between σ and the mean V^0 is readily apparent here and is due to the shallowness of our photometry. The last row of this table gives the parameters of the "best-fit" Gaussian for our data: $\sigma = 1.73$, $V^0 = 24.2$; however, it is clear that a wide range of σ (and V^0) will give comparable fits to the data. (Note that the two magnitude bins with values of $\phi(V)$ in parentheses in Table 9 have been excluded from the fitting process.)

Given that our background LF is significantly contaminated by part of the M87 GCS, it is worthwhile to attempt a "cleaning" of this function to check on the validity of our

TABLE 9

THE M87 GCLF

V	N_{obs} ($R \leq 6'.82$)[a]	N_b ($R \geq 6'.82$)[b]	$N_{cl} \equiv \phi(V)$ ($R \leq 6'.82$)
19.00–19.25.....	6 ± 2.5	2 ± 1.4	(−2.27 ± 3.77)
19.25–19.50.....	4 ± 2.0	0	4.00 ± 2.00
19.50–19.75.....	10 ± 3.2	1 ± 1.0	5.87 ± 3.77
19.75–20.00.....	14 ± 3.8	1 ± 1.0	9.87 ± 4.27
20.00–20.25.....	26 ± 5.1	3 ± 1.7	13.60 ± 6.22
20.25–20.00.....	34 ± 5.8	2 ± 1.4	25.73 ± 6.50
20.50–20.75.....	59 ± 7.7	0	(59.00 ± 7.70)
20.75–21.00.....	66 ± 8.1	6 ± 2.4	41.19 ± 9.55
21.00–21.25.....	92 ± 9.6	5 ± 2.2	71.33 ± 10.63
21.25–21.50.....	109 ± 10.5	11 ± 3.3	63.52 ± 12.48
21.50–21.75.....	146 ± 12.1	13 ± 3.6	92.25 ± 14.15
21.75–22.00.....	160 ± 12.7	16 ± 4.0	93.85 ± 15.06
22.00–22.25.....	179 ± 13.4	17 ± 4.1	108.70 ± 15.84
22.25–22.50.....	235 ± 15.4	21 ± 4.6	148.20 ± 18.04
22.50–22.75.....	275 ± 16.8	23 ± 4.8	179.90 ± 19.43
22.75–23.00.....	291 ± 17.5	34 ± 5.9	149.40 ± 21.18
23.00–23.25.....	390 ± 20.5	40 ± 6.5	218.60 ± 24.27
23.25–23.50.....	441 ± 22.5	51 ± 7.9	223.40 ± 27.07
23.50–23.75.....	514 ± 27.1	74 ± 10.6	201.80 ± 34.68
23.75–24.00.....	587 ± 33.6	66 ± 12.0	304.10 ± 41.26
$\sum N$	3638 ± 68	386 ± 23	2042 ± 82

[a] Area 123.06 arcmin^2.
[b] Area 29.76 arcmin^2.

TABLE 10

GCLF PARAMETERS

σ	V^0	A	χ^2
1.50.....	23.65	216.28	1.01
1.60.....	23.87	227.81	0.88
1.70.....	24.11	242.63	0.83
1.80.....	24.37	261.15	0.83
1.90.....	24.65	283.90	0.88
2.00.....	24.94	311.60	0.96
2.10.....	25.25	345.15	1.05
1.73.....	24.18	247.77	0.82

derived GCLF parameters. To do this, we have applied the formalism of Butterworth & Harris (1992), in which the "first-order" GCLF (col. 4 of Table 9) is scaled down to the total population of ~200 globular clusters expected in the background on the basis of the GCS radial profile, and then subtracted from the first-order background LF (col. 3 of Table 9) to yield a "cleaned" luminosity distribution for the background area. This improved background is then scaled appropriately, and subtracted from the original, raw LF (i.e., col. 2 of Table 9). Upon doing this, we repeat the Gaussian fits and find that an even wider range of σ is allowed because of the extra noise that this process introduces to the distribution, but that the best fit is not significantly altered; specifically, the Gaussian parameters which yield a minimal χ^2 statistic turn out to be $\sigma = 1.69$ and $V^0 = 24.1$.

In Figures 16 and 17 we plot the background LFs (both raw and cleaned) and the GCLF which we obtained. In Figure 18, we show the *luminosity-weighted luminosity function* (LWLF; Harris 1991)

$$\psi(V) = \text{const} \times 10^{-0.4V}\phi(V)\,, \qquad (15)$$

which describes the relative contribution of the clusters in each magnitude bin to the total light emitted by the M87 GCS. For definiteness, we take the Virgo distance modulus to be $(m - M)_0 = 31.4$ in evaluating the constant in equation (15) (see below). If $\phi(V)$ is a Gaussian with mean V^0 and dispersion σ, then $\psi(V)$ is also a Gaussian with dispersion σ, but with mean $V^1 = V^0 - 0.4\sigma^2 \ln 10$. In cases such as ours, the peak V^1 of the LWLF is easily seen even if the GCLF peak V^0 is not, and it provides another way to estimate functional parameters. Thus, we have transformed our Gaussian fits to $\phi(V)$ and compared them to the data for $\psi(V)$. Clearly, although larger values of σ (and fainter V^0) give adequate formal fits to the data, the agreement is not good at the brightest (albeit least populous) end of the GCLF for $\sigma \gtrsim 1.9$; similarly, it appears that values of σ less than about 1.5 would probably give acceptable agreement with the brightest tail of the GCLF, but would fail to describe the fainter, more heavily populated part.

Finally, then, we conclude that the bright half of the M87

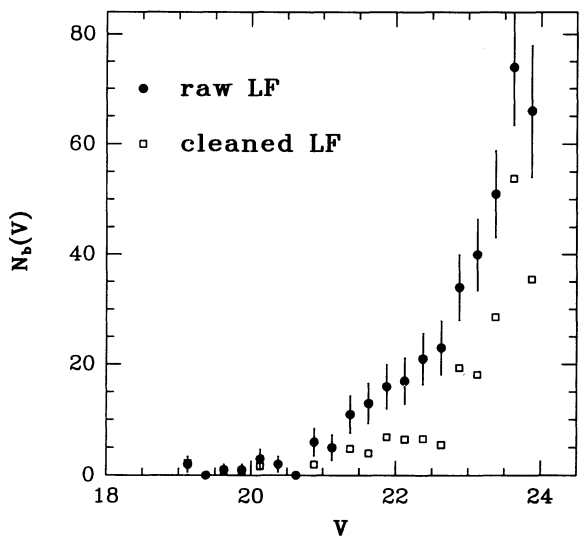

FIG. 16.—Luminosity distribution of objects in our background region ($R \geq 6'.82$), both before and after the cleaning process described in the text.

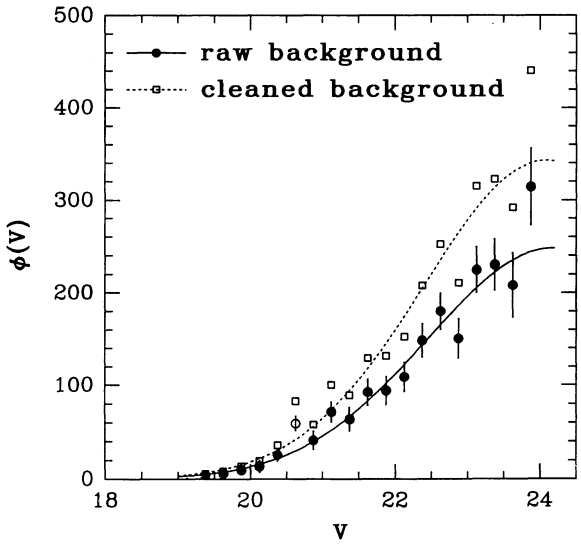

FIG. 17.—M87 GCLF, defined as the luminosity distribution of objects interior to $R = 6'.82$, after subtracting each of the background LFs of Fig. 16. The filled circles describe the distribution after subtracting the contaminated background function (the open circle has been excluded from the Gaussian fit), and the open squares correspond to subtraction of the cleaned background. Overlaid on the distributions are the best-fit Gaussians for each case; their parameters are given in the text.

GCLF is reasonably described by a Gaussian of dispersion between 1.5 and 1.9 and corresponding turnover V^0 between 23.7 and 24.6; again, the best-fit Gaussian has $\sigma \simeq 1.7$ and $V^0 \simeq 24.2$. Thus, if we attach (somewhat arbitrarily) an uncertainty of ± 0.4 mag to the V^0 value; assume that the true absolute magnitude of the GCLF turnover matches that of the Milky Way GCS ($M_V^0 = -7.29 \pm 0.13$; Secker 1992); consider the uncertainty in our photometric zero point (± 0.05 mag; § 2.1); and take the foreground absorption toward Virgo to be

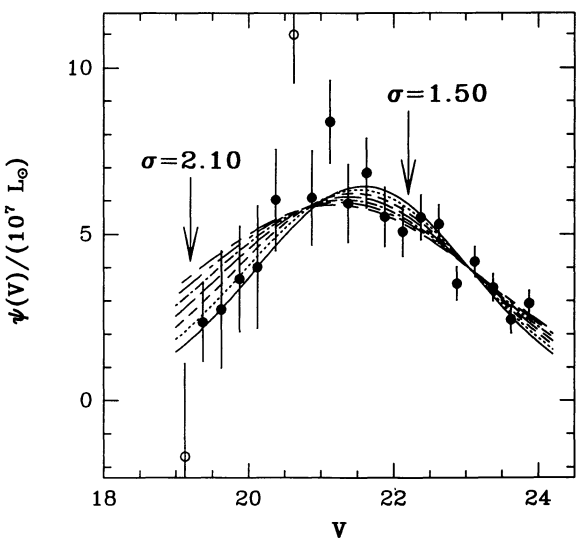

FIG. 18.—Luminosity-weighted luminosity function of the M87 GCS. A Virgo distance modulus of 31.4 has been assumed for normalization, and the GCLF given in Table 9 has been used. The open circles mark points that have been excluded from the functional fits; note that the excluded point at $V = 20.625$ is anomalously "bright" because statistical fluctuations cause the background population to go to 0 in that bin. The curves are Gaussians with $\sigma = 1.5$ to 2.1 (in steps of 0.1) and corresponding V^0, A as in Table 10.

$A_V = 0.07$ mag (using $E(B-V) = 0.023$ from Burstein & Heiles 1984); then we obtain a true Virgo distance modulus of

$$(m - M)_0 = 31.4 \pm 0.4 , \quad (16)$$

a result which, within the uncertainty, barely agrees with a weighted mean Virgo modulus of 30.80 ± 0.19 from six independent distance determinations (Jacoby et al. 1992).

Secker & Harris (1993) analyzed the data of Harris et al. (1991) to find $\langle V^0 \rangle = 23.8 \pm 0.2$ and $\langle \sigma \rangle = 1.4 \pm 0.1$ for the GCLFs of three Virgo gE's (NGC 4365, 4472, and 4649). A comparison with our M87 results (Table 10) shows that the two turnover magnitudes are consistent with each other, but perhaps gives the impression that the M87 GCLF is broader than that of the Virgo ellipticals; as well, even though our data are marginally consistent with a GCLF dispersion of 1.5 for M87, the data of van den Bergh et al. (1985) also suggest $\sigma \simeq 1.7$ (Hanes & Whittaker 1987; Harris et al. 1991). Nevertheless, Harris et al. (1991) performed two-sample Kolmogorov-Smirnov tests to compare the M87 GCLF of van den Bergh et al. (1985) with those of the Virgo gE's, and found no statistically significant differences between them. Since the van den Bergh et al. GCLF is statistically indistinguishable from ours (see below), this conclusion must stand; even though $\sigma = 1.7$ is probably better than $\sigma = 1.5$ as a description of the M87 GCLF alone, we will require deeper photometry allowing for a more secure determination of the parameters before any firm conclusions can be made regarding the significance of any differences between the M87 and Virgo gE GCLFs.

5.2. *The GCLF as a Function of Radius*

The possibility that the present-day members of GCSs may represent only a fraction of the initial population of these systems has attracted much attention in recent years. Theoretical arguments and numerical simulations suggest that many dynamical processes may disrupt individual globular clusters (e.g., disk/bulge shocking, dynamical friction, evaporation, collisional encounters with massive black holes in galactic halos), perhaps destroying a significant portion of the original GCS in the Milky Way (Aguilar, Hut, & Ostriker 1988), in M87 (Ostriker et al. 1989), and indeed in most galaxies (see the review of Harris 1991). With this in mind we have examined the M87 GCLF separately in each of the four annuli of the last section, to search for any evidence of such dynamical evolution of the GCS.

In Table 11 we present the GCLFs in each of these annuli (as obtained from an "impure" background subtraction); in Figure 19, we scale these four GCLFs to have the same total *number* of objects (514) as found in the innermost annulus, and compare them to the scaled best-fit Gaussian obtained for the entire sample (Table 10). All four LFs follow this mean curve, but with a scatter which increases toward larger galactocentric radius; this scatter is due to the larger relative uncertainty induced by the background subtraction in the outer regions. In addition, in any given magnitude bin (with the exception of the two faintest), the corresponding point for any one annular LF lies within 1 σ of the other three; this suggests that *if* there is a significant radial variation in the M87 GCLF in this region, it must occur only at the fainter end of the distribution.

In order to quantify the degree of agreement (or disagreement) between the annular GCLFs, we apply the Kolmogorov-Smirnov (KS) two-sample test to each of the six pairs of LFs resulting from our division of the GCS. To do this, we form the cumulative (luminosity) distribution function (CDF) in each annulus and use the absolute value of the maximum separation between any pair of CDFs (Δ_{max}) and the effective number of the combined sample ($N_{eff}^{-1} \equiv m_1^{-1} + m_2^{-1}$,

TABLE 11

THE M87 GCLF AS A FUNCTION OF RADIUS

	$\phi(V)$			
V	$1'.21 \le R \le 1'.87$[a]	$1'.87 \le R \le 2'.88$[b]	$2'.88 \le R \le 4'.43$[c]	$4'.43 \le R \le 6'.82$[d]
19.00–19.25.....	0.58 ± 1.00	−1.00 ± 0.71	−1.38 ± 1.96	−0.47 ± 3.74
19.25–19.50.....	0	2.00 ± 1.41	1.00 ± 1.00	1.00 ± 1.00
19.50–19.75.....	2.79 ± 1.75	−0.50 ± 0.50	0.81 ± 1.85	2.76 ± 3.18
19.75–20.00.....	0.79 ± 1.02	3.50 ± 2.06	1.81 ± 2.11	3.76 ± 3.32
20.00–20.25.....	3.36 ± 2.03	2.50 ± 2.18	0.44 ± 2.89	7.29 ± 5.41
20.25–20.50.....	5.58 ± 2.47	5.00 ± 2.55	9.62 ± 3.85	5.53 ± 4.47
20.50–20.75.....	12.00 ± 3.46	13.00 ± 3.62	20.00 ± 4.49	14.00 ± 3.75
20.75–21.00.....	9.73 ± 3.40	16.01 ± 4.54	13.87 ± 5.43	1.58 ± 6.71
21.00–21.25.....	12.94 ± 3.77	17.51 ± 4.61	24.06 ± 6.09	16.82 ± 7.30
21.25–21.50.....	18.67 ± 4.72	20.51 ± 5.41	17.93 ± 6.82	6.40 ± 9.27
21.50–21.75.....	19.24 ± 4.75	25.52 ± 5.94	30.55 ± 8.03	16.93 ± 10.57
21.75–22.00.....	24.61 ± 5.36	22.02 ± 5.90	26.99 ± 8.28	20.22 ± 11.66
22.00–22.25.....	32.40 ± 6.09	18.52 ± 5.60	30.80 ± 8.69	26.98 ± 12.28
22.25–22.50.....	24.55 ± 5.52	48.53 ± 8.06	46.05 ± 10.08	29.04 ± 13.52
22.50–22.75.....	40.12 ± 6.89	34.53 ± 7.29	58.67 ± 10.97	46.57 ± 14.72
22.75–23.00.....	42.79 ± 7.60	43.05 ± 8.42	39.60 ± 11.49	24.97 ± 16.73
23.00–23.25.....	48.52 ± 8.35	56.05 ± 9.65	70.47 ± 13.56	49.55 ± 18.98
23.25–23.50.....	47.19 ± 8.52	45.57 ± 9.91	65.40 ± 15.02	71.95 ± 22.89
23.50–23.75.....	76.31 ± 13.16	64.10 ± 12.69	45.08 ± 18.12	22.52 ± 28.73
23.75–24.00.....	91.01 ± 16.32	87.09 ± 16.14	42.58 ± 19.63	93.41 ± 34.39
$\sum N$	514	524	545	461
$\sum (N/\sigma)^2$	339	305	213	78

[a] Area 6.31 arcmin^2.
[b] Area 14.84 armin^2.
[c] Area 35.36 armin^2.
[d] Area 66.55 armin^2.

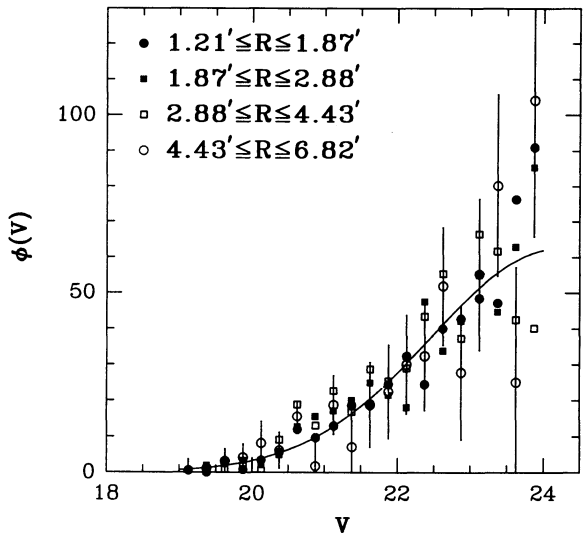

FIG. 19.—GCLF in four different circular annuli. The solid curve is the Gaussian which best fits the entire GCLF (i.e., 1′.21 ≤ R ≤ 6′.82); its parameters are $\sigma = 1.73$, $V^0 = 24.2$. This curve and all the observed functions have been scaled to reflect a total population of 514 globulars (i.e., the number of objects in the innermost annulus). In the interests of clarity, error bars have been plotted only for the outermost annulus.

where m_1, m_2 are the populations of the individual annuli) to find the KS statistic $D_N = (N_{\rm eff})^{1/2}\Delta_{\rm max}$. The probabilities that the null hypothesis is true (i.e., that the two GCLFs of a given pair are drawn from the same parent population) are then computed from the formula for the asymptotic (in the limit of large $N_{\rm eff}$) distribution of D_N (e.g., Press et al. 1992, p. 618). Strictly speaking, the KS test is applicable only to *unbinned* data. However, in constructing the GCLF, we did bin the data in order to apply the photometric completeness corrections and statistically subtract the background LF. Thus, the D_N statistic found by considering the binned CDFs can only be an approximation to the true statistic. (Of course, this approximation should be quite good for sufficiently narrow bin size, and in the limit of infinitesimal bin width, the test will be exact.) In addition, the KS test *assumes* Poisson errors in the distributions in question (see Breiman 1968, p. 284ff.); but the errors in the GCLF come from a combination of $(N)^{1/2}$ statistics, completeness errors, and background uncertainties and can be significantly non-Poisson. To deal with this, we redefine the total population of each of our annuli as $m' \equiv \sum_i (N_i/\sigma_i)^2$, where the sum runs over the magnitude bins; then we use $N'_{\rm eff} \equiv m'_1 m'_2/(m'_1 + m'_2)$ as the effective sample size to be used in calculating the D_N statistic. (Note that in the limit of Poisson errors, we have $\sigma_i = (N_i)^{1/2}$, and our revised m'_1, m'_2 become the true sample sizes.) This definition has the advantage of effectively decreasing the numbers of objects in the fainter magnitude bins in each annulus, and in the outer radial zones in general; thus less statistical weight is given to any differences in the more uncertain CDFs from these regions.

In Figure 20 we plot the cumulative GCLFs in each of our four annuli, where we have cut the distributions off at $V = 20$ in order to avoid negative populations in the brightest bins due to the background subtraction. The results of the KS test applied to these functions are recorded in Table 12, in the form of probabilities that the null hypothesis is true; they have been calculated using both the standard definition of $N_{\rm eff}$ and our revised version.

Inspection of Figure 20*a* suggests very close agreement among the GCLFs for $V \leq 23$. This conclusion is supported by the KS probabilities of Table 12, and is consistent with the previous studies of Strom et al. (1981), Grillmair et al. (1986), Lauer & Kormendy (1986), and Cohen (1988), all of whom found no significant radial variation of the M87 GCLF in this magnitude range. It is perhaps interesting that there seems to be a radial trend of the KS probabilities, in the sense that a given annular LF agrees better with other LFs which are closer to it; but this is not a statistically significant result.

When we extend the comparison to include the fainter magnitudes (Fig. 20*b*), there appears to be a relative excess of bright objects in the annulus 2′.88 ≤ R ≤ 4′.43, while the GCLFs from the other three annuli are rather similar to each other. Again, the probabilities in Table 12 reflect this situation. However, a look at Figure 19 suggests that the reason for this is the low number of clusters found in the very last magnitude bin of this one annulus (and indeed, when the cumulative GCLFs are formed for $20 \leq V \leq 23.75$ only, and the KS tests done with $m = \sum_i (N_i/\sigma_i)^2$, the distribution in this annulus comes back in line with the others: the probability of the null hypothesis for the pairing of annuli 1 and 3 becomes 0.25; for annuli 1 and 4, 0.40; and for all other comparisons, >0.8).

Thus, we conclude that for 1′.21 ≤ R ≤ 6′.82 and $20 \leq V \leq 23.75$ (and probably for $V \leq 24$), the M87 GCLF exhibits no significant variation with galactocentric radius. (This is complementary to our finding [§ 3] that the GCS radial profile shows no dependence on magnitude.) The χ^2 two-sample test (Press et al. 1992, p. 614ff.) has also been applied to these data and shows a good agreement among the LFs of all four annuli. Finally, then, we compare our entire GCLF with that of van den Bergh et al. (1985), which applies to the region 0′.3 ≲ R ≲ 2′. To do this, we take the Gaussian curve which best fits their LF ($\sigma = 1.70$, $V^0 = 24.0$, according to Harris et al. 1991) and use it as a model against which to contrast our data. Not surprisingly, given that the Gaussian

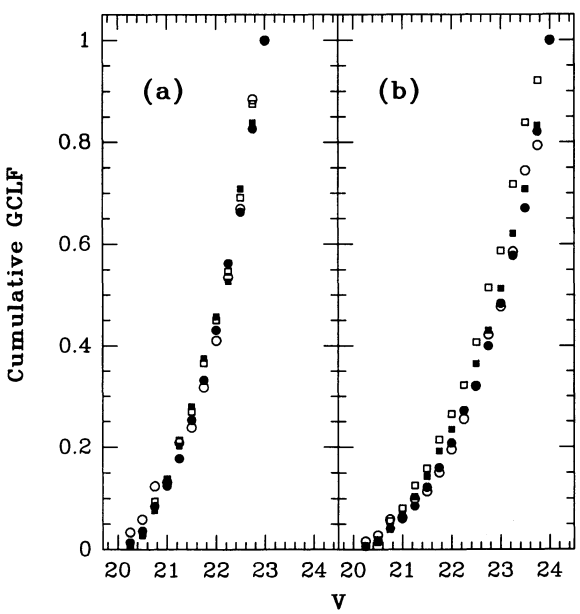

FIG. 20.—Cumulative GCLFs of four separate annuli (the various point types label the different annuli as in Fig. 19), in the two magnitude intervals (*a*) $20 \leq V \leq 23$ and (*b*) $20 \leq V \leq 24$.

TABLE 12

KOLMOGOROV-SMIRNOV COMPARISON OF ANNULAR GCLFs

	$20 \le V \le 23$								$20 \le V \le 24$							
	$m = \sum N$				$m = \sum (N/\sigma)^2$				$m = \sum N$				$m = \sum (N/\sigma)^2$			
ANNULUS	1	2	3	4	1	2	3	4	1	2	3	4	1	2	3	4
1.....	1.00	0.95	0.88	0.82	1.00	0.98	0.98	1.00	1.00	0.71	8e-7	0.15	1.00	0.92	1e-3	0.90
2.....	...	1.00	0.99	0.81	...	1.00	1.00	1.00	...	1.00	3e-4	0.71	...	1.00	0.03	1.00
3.....	...	...	1.00	0.92	...	...	1.00	1.00	...	...	1.00	4e-4	...	...	1.00	0.29
4.....	...	...	...	1.00	...	...	...	1.00	...	...	...	1.00	...	...	...	1.00

NOTES.—Annulus 1: $1'.21 \le R \le 1'.87$; Annulus 2: $1'.87 \le R \le 2'.88$; Annulus 3: $2'.88 \le R \le 4'.43$; Annulus 4: $4'.43 \le R \le 6'.82$.

parameters are very close to our own best fit, a KS *one*-sample test returns a probability of 0.83 that the two distributions are the same; hence we can say that there is no evidence of a radial variation in the bright half of the M87 GCLF over the region $0'.3 \lesssim R \lesssim 6'.8$ ($1.4 \lesssim R \lesssim 31.4$ kpc for $(m - M)_0 = 31.0$). It is especially important to note that the GCLF of the cD envelope of M87 agrees very well with that of the inner body of the galaxy.

Although this result is not a trivial one, neither is it surprising. In fact, the numerical experiments of Aguilar et al. (1988) and Ostriker et al. (1989) indicate that the destruction mechanisms opertating on globular clusters are generally most efficient within galactocentric radii of $\lesssim 4$ kpc ($R < 1'$ at the distance of M87), so our negative detection may just be a reflection of the stability of the outer-halo GCS against these processes. Also, the observations to date cover only the brightest half (at most) of the GCLF; the fainter, smaller globulars may be far more affected by dynamical destruction mechanisms, without the distribution of the larger, brighter clusters showing any sign of change. At the same time, it is perhaps worrisome that it is so difficult to detect the signature of these theoretically powerful dynamical effects (Harris et al. 1991 similarly find no significant variation of the GCLFs in NGC 4365, 4472, and 4649 over the range $30'' \le R \le 140''$ and $20 \lesssim V \lesssim 25.5$). It would thus be of great interest to examine the radial behavior of the fainter half of the M87 GCLF at small galactocentric distances, where the good statistics afforded by the large sample size may finally show us what effect (if any) dynamical evolution has had on the overall luminosity distributions of GCSs. Multicolor imaging data for the central regions of M87 have recently been obtained with the CFHT and are currently under analysis.

6. THE TOTAL POPULATION AND SPECIFIC FREQUENCY

The specific frequency S_N of a GCS is defined as the number of globular clusters per unit halo light, normalized to a galaxy luminosity of $M_V^T = -15$: $S_N = N_t \times 10^{0.4(M_V^T + 15)}$ (Harris & van den Bergh 1981). This ratio is largely an indication of the cluster formation efficiency in a given region and differs among E galaxies by an order of magnitude.

We have calculated the run of this parameter with galactocentric radius for the M87 GCS; the results are given in Table 13. (Note that the last row of this table shows that over the region $1'.21 \le R \le 9'.09$, the light of the cD envelope constitutes $\sim 8\%$ of the total flux, and the number of globular clusters in the envelope likewise represents $\sim 9\%$ of the total GCS population.) For each annulus, the quoted number of clusters applies to the magnitude interval $20 \le V \le 24$, and the total luminosity of the annulus is calculated in B from the surface brightness profile of de Vaucouleurs & Nieto (1978, hereafter

TABLE 13

SPECIFIC FREQUENCIES OF THE M87 GCS

	OBSERVED (O)[a]			GALAXY (C)[b]			cD ENVELOPE ($O-C$)		
ANNULUS	N_{cl}	B	S_N	N_{cl}	B	S_N	N_{cl}	B	S_N
$1'.21 \le R \le 1'.40$.....	166 ± 16	13.07	9.9 ± 1.0	154 ± 8	13.16	10.0 ± 0.5	12 ± 18	15.82	...
$1'.40 \le R \le 1'.62$.....	169 ± 17	13.09	10.2 ± 1.0	170 ± 8	13.14	10.8 ± 0.5	1 ± 19	16.46	...
$1'.62 \le R \le 1'.87$.....	224 ± 19	13.11	13.8 ± 1.2	183 ± 6	13.15	11.7 ± 0.4	41 ± 20	16.71	...
$1'.87 \le R \le 2'.16$.....	189 ± 17	13.12	11.8 ± 1.1	200 ± 5	13.14	12.7 ± 0.3	−11 ± 18	17.47	...
$2'.16 \le R \le 2'.49$.....	192 ± 17	13.16	12.4 ± 1.1	212 ± 3	13.17	13.8 ± 0.2	−20 ± 18	18.25	...
$2'.49 \le R \le 2'.88$.....	247 ± 20	13.12	15.4 ± 1.3	232 ± 1	13.16	15.0 ± 0.1	15 ± 20	16.72	...
$2'.88 \le R \le 3'.32$.....	242 ± 19	13.20	16.2 ± 1.3	240 ± 2	13.22	16.4 ± 0.1	2 ± 19	17.55	...
$3'.32 \le R \le 3'.83$.....	262 ± 20	13.19	17.4 ± 1.3	254 ± 5	13.26	18.0 ± 0.4	8 ± 21	16.20	...
$3'.83 \le R \le 4'.43$.....	274 ± 22	13.28	19.8 ± 1.6	270 ± 8	13.30	19.9 ± 0.6	4 ± 24	17.63	...
$4'.43 \le R \le 5'.11$.....	350 ± 27	13.20	23.5 ± 1.8	274 ± 10	13.40	22.1 ± 0.8	76 ± 29	15.14	30 ± 12
$5'.11 \le R \le 5'.90$.....	380 ± 33	13.10	23.3 ± 2.0	282 ± 15	13.48	24.5 ± 1.3	98 ± 37	14.42	20 ± 8
$5'.90 \le R \le 6'.82$.....	378 ± 36	13.14	24.0 ± 2.3	288 ± 20	13.57	27.2 ± 1.9	90 ± 42	14.35	17 ± 8
$6'.82 \le R \le 7'.87$.....	364 ± 49	13.30	26.8 ± 3.6	286 ± 23	13.70	30.4 ± 2.5	78 ± 54	14.58	19 ± 13
$7'.87 \le R \le 9'.09$.....	292 ± 95	13.31	22 ± 7	286 ± 25	13.83	34.3 ± 3.0	6 ± 99	14.36	...
Totals.....	3729 ± 133	10.30	17.3 ± 0.6	3326 ± 80	10.45	17.7 ± 0.4	342 ± 83[c]	13.08[c]	21 ± 5[c]

[a] N_{cl} is computed from the surface density profile of McLaughlin et al. 1993, using the full area of each annulus; B is computed from the halo light profile of dVN.

[b] Calculated from the best-fit $R^{1/4}$-law profiles for $R \le 4'.5$ (eq. [6a] of the text for the GCS, and eq. [1] of dVN for the halo light).

[c] These totals apply only to $4'.43 \le R \le 7'.87$.

dVN); in each case, the numbers are computed as though the entire annulus were observed. To obtain S_N from this, several assumptions are made: we suppose the *entire* GCLF to be well described by a Gaussian with $V^0 = 24.2$ and $\sigma = 1.73$ so that with our magnitude limits, the fraction of the GCS seen in any annulus is $\simeq 0.45$; the color of the M87 halo light is taken to be constant at $(B-V) = 1.0$ (Carter & Dixon 1978); and the visual distance modulus of Virgo is set at $(m - M)_V = 31.0 \pm 0.2$ (based on a weighted mean of the true distance moduli obtained by Jacoby et al. 1992 and by our GCLF analysis). The quoted errors in S_N reflect only the uncertainties of the number counts.

The numbers of Table 13 apply only to the radial regimes listed there. However, it is also of interest to know the total population of the GCS over all radii, and the associated global specific frequency of M87. We first integrate the best-fit de Vaucouleurs profile for the GCS inside 4.5 (eq. [6a]) from $R = 1.2$ to 25′, which is a reasonable estimate of the "edge" of the galaxy (e.g., dVN). This gives $N_{\rm cl}(1.2\text{–}25') \simeq 5050 \pm 400$. To this we add 500 ± 100 clusters to account for the $\sim 10\%$ excess found in the cD envelope, and another 500 ± 100 clusters to represent the population of the core of the GCS (Lauer & Kormendy 1986) (we assume here that $\sigma_{\rm core} \approx 106$ arcmin^{-2} for $0 \leq R \leq 1.2$ [MHH]). The total population of the M87 GCS over all magnitudes is then $N_t \simeq 13{,}450 \pm 950$. Using $B^T = 9.57$ for the galaxy (dVN), and making the same assumptions as before, we finally have $S_N(\mathrm{M87}) = 14.3 \pm 1.0$. The quoted error is solely due to the variance of the number counts and does not reflect the uncertainty in our GCLF parameters and the adopted distance modulus. Nevertheless, this result is in excellent agreement with that of Harris (1986; $S_N = 14 \pm 3$).

It is evident from Table 13 (and Fig. 21) that the *local* $S_N(R)$ increases strongly with radius, reflecting the near flatness of the GCS radial profile in the inner regions, and its overall shallower falloff compared with the halo light. If we consider only the area $1.5 \leq R \leq 25'$, we obtain $N_{\rm cl} \simeq 5300 \pm 350$ ($N_t \simeq 11{,}755 \pm 775$) and $B = 10.22$, and hence $S_N(R \geq 1.5) = 22.9 \pm 1.5$; this may be a more accurate indication of the *initial* specific frequency of the M87 GCS, exclusive of the dynamical effects that may have strongly affected the innermost zone.

The specific frequencies we find may still be lower limits to the true values since (1) we may have overestimated the background surface density by some 25% (§ 3), and (2) the GCLF dispersion we have adopted (1.73) is rather broader than the value $\sigma = 1.5$ used in the past, and thus a relatively higher fraction of the GCS is placed in the observed brighter part of the distribution (for fixed V^0), making the correction factor for N_t smaller. For any other combination of $(m - M)_V$, V^0, and σ, our S_N should be multipled by the correction factor

$$\gamma = \frac{0.89}{\mathrm{erf}\,[(V^0 - 20)/\sqrt{2}\,\sigma] - \mathrm{erf}\,[(V^0 - 24)/\sqrt{2}\,\sigma]} \times 10^{0.4[31.0-(m-M)V]}. \quad (17)$$

The first factor in this expression corrects the predicted total number of clusters for different sets of GCLF parameters, and the second term corrects the galaxy's true luminosity for different distance moduli. In particular, if we keep $V^0 = 24.2$ and $\sigma = 1.73$ but include the uncertainty of ± 0.2 mag in our distance modulus, then $\gamma \simeq 1 \pm 0.2$, so that the net specific frequency becomes $S_N(\mathrm{M87}) = 14 \pm 4$.

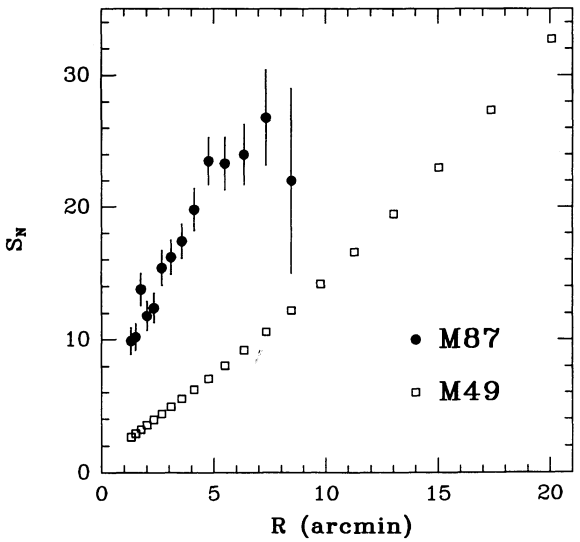

FIG. 21.—Run of S_N with galactocentric radius for M87 (*filled circles*; data from Table 13) and M49 (*open squares*). Points are plotted at the geometric mean radius of each annulus. The calculations for M49 are made by integrating the best-fit de Vaucouleurs profiles of the cluster system ($\log a_1 = 3.32$, $a_2 = 1.76$; Harris 1986) and the halo light ($\mu_B = 14.707 + 2.517R^{1/4}$, from the data of King 1978), and then correcting for incompleteness by taking $V^0 = 23.9$, $\sigma = 1.50$ for the M49 GCLF (Harris et al. 1991) and using $V_{\rm lim} = 23.3$ for the study of Harris (1986); the color of M49 is taken to be $(B-V) = 1.0$, and its distance modulus is set at $(m - M)_V = 31.0$, just as in the calculations for M87.

6.1. *The High-S_N Phenomenon and cD Envelopes*

The average S_N of all other measured Virgo ellipticals is ~ 5 (Harris 1991), so the M87 GCS is overabundant by a factor of about 3. Moreover, this overabundance persists, to the same extent, throughout the entire M87 halo. To illustrate this, we plot in Figure 21 the observed specific frequencies of M87 from Table 13, and the $S_N(R)$ calculated for M49 = NGC 4472 (a more "normal" giant elliptical) over a larger range of radius.

Although exceptional, the occurrence of high S_N is by no means unique to the M87 GCS; several (but not all) centrally dominant gE/cD galaxies in other clusters show the same phenomenon. Some attempts have been made to explain this feature in terms of galactic evolution in a cluster environment. Forte, Martinez, & Muzzio (1982) first suggested that large numbers of "extra" globulars could be collisionally stripped from smaller cluster members and accreted onto a central supergiant *after* star formation; a different suggestion (e.g., Fabian, Nulsen, & Canizares 1984) is that the excess globulars condense out of cooling flows around the central galaxy. Van den Bergh (1984) makes several arguments against the first scenario for the case of M87 in particular, but perhaps the most effective objection is that such stripping of smaller galaxies (with normal $S_N \lesssim 5$) must take both globular clusters and halo field stars in the same proportion in which they are found, so that while this process can increase the total *population* of the accreting galaxy's GCS, it cannot increase it specific frequency, nor explain the high S_N in the inner regions of M87. The cooling flow scenario runs into the severe obstacle of no correlation between S_N and the size of the X-ray halo (in particular, NGC 6166, with a vastly larger X-ray halo than M87, has $S_N \simeq 4$, which is just normal; see Pritchet & Harris 1990 and Bridges, Hanes, & Harris 1991). Another approach, suggested by the descriptive modeling of Ashman & Zepf

(1992), is that globular clusters may form efficiently during mergers of gas-rich pregalactic fragments, and that dominant central galaxies like M87 underwent much higher rates of these events. (However, this prompts the question of why some centrally dominant galaxies do *not* have a high S_N; we will return to this point shortly.)

All of this suggests that perhaps high-S_N GCSs were always so. A comparison of the specific frequencies of all centrally dominant galaxies studied to data may help to strengthen this conclusion, so in Table 14 we present some relevant data on the parent clusters of these galaxies. In general, the galaxies represented in this table can be said to fall into two distinct groups: one with $S_N \sim 15$, and one with $S_N \simeq 4$. Oddly though, NGC 3842, the brightest member of A 1367, has $S_N \simeq 7$–8; it is not immediately obvious whether this should be considered a high-S_N system or a more normal one. However, Butterworth (1991) states that correction for a combination of observational effects (background estimation, uncertainties in the form of the GCLF, and possible differences between the radial profiles of the M87 and NGC 3842 GCSs) could drive the specific frequency of this galaxy up to ~ 12; in particular, he assumes $\sigma(\mathrm{GCLF}) = 1.4$ for M87 and NGC 3842 alike, whereas we now find $\sigma(\mathrm{M87}) \simeq 1.7$. Moreover, a direct integration of the best-fit de Vaucouleurs profile for the NGC 3842 GCS out to $R = 5'$ (equivalent to $R = 25'$ at the distance of Virgo) yields (after correcting for the fraction of the GCS left unseen in their survey) $S_N(\mathrm{NGC\ 3842}) \sim 9$–13 (see Butterworth & Harris 1992). In the following discussion, we take the view that NGC 3842 may then be a high-S_N system (although perhaps only marginally so); further (deeper) observations of its GCS would help to clear this point up.

The second column of Table 14 lists the Abell (1958) richness class of each cluster. Malumuth & Richstone (1984) have shown that the efficiency of collisional stripping in a virialized cluster increases with richness, so that if the scenario of Forte et al. (1982) were correct, we might expect to find the S_N of central galaxies also increasing with cluster richness. However, inspection of the last column of the table shows that there is no such correlation.

In the third column of Table 14 we list the global morphological fractions of galaxies in most of the clusters, as a couple of simple arguments would seem to suggest that there might be some relation between this cluster characteristic and the S_N of the central galaxy. Ashman & Zepf (1992) and Kumai, Basu, & Fujimoto (1993) propose that $\gtrsim 10^{12}\ M_\odot$ of gas may have been torn from galaxies which merged with M87 early in the latter's history (i.e., in the first few Gyr) to (preferentially) form $\gtrsim 10^4$ "extra" globulars. If such a process can explain the high-S_N phenomenon in general, it would seem that those clusters containing high-S_N galaxies should have had a relatively higher proportion of gas-rich constitutents at such early times, as compared to those clusters with low-S_N central galaxies. So if, as Kumai et al. (1993) explicitly assume for Virgo, the present-day morphological fractions of clusters reflect the initial galaxy content (Oemler 1974; Dressler 1980), we may expect to see a correlation between clusters' spiral fractions and the S_N of their central galaxies. On the other hand, the proportions of different types of galaxies in galaxy clusters may be more affected by their subsequent evolution (e.g., Whitmore, Gilmore, & Jones 1993). Then since the growth of a central galaxy's S_N presumably comes at the expense of gas-rich systems, we might instead see an anticorrelation of Sp/(E+S0+Sp) with S_N. However, neither of these trends is obvious in the data of Table 14 (compare especially A 1656 and A 2199, which have the same Abell richness and almost identical galaxy content, but whose central galaxies' S_N differ by a factor of 3). To be sure, it may be rather more correct to compare S_N with the *local* spiral fractions near the galaxy in question. But it seems rather difficult to separate the effects of initial conditions from those of subsequent evolution in predicting what we should see today; it may be that the initial conditions around a young central cluster galaxy are not well represented by *any* present-day cluster properties. In short, there seems to be no quick, definitive way to compare the ideas of Ashman & Zepf (1992) and Kumai et al. (1993) (which are admittedly rather qualitative) with the observations of S_N; nevertheless, an attractive aspect of these scenarios is their allowance for the in situ formation of any "excess" globular clusters (this is an apparently unavoidable requirement, at least in the case of M87; see van den Bergh 1984). Also, they imply that a high S_N is imparted to a galaxy very early on in its life.

Finally, in column (4) of Table 14, we give the Bautz &

TABLE 14

SPECIFIC FREQUENCIES OF CENTRAL gE/cD GALAXIES

Cluster	Richness[a]	E:S0:Sp	BM Class[a]	Galaxy	S_N
Virgo	1	14:19:67[d]	III	NGC 4486	14 ± 4
Fornax	1	30:27:43[d]	II–III	NGC 1399	16 ± 4[i]
A 1060	1	10:35:55[e]	III	NGC 3311	18 ± 6[j]
A 1367	2	17:40:43[f]	II–III	NGC 3842	7 ± 3[k]
A 1656	2	35:47:18[f]	II	NGC 4874	12 ± 6[l]
A 2052	0	...	II	UGC 9799	20 ± 6[m]
A 2107	1[b]	...	I[b]	UGC 9958	13 ± 6[m]
A 2199	2	35:41:24[f]	I	NGC 6166	4 ± 2[n]
A 2666	0	20:37:43[e]	I–II	NGC 7768	4 ± 2[m]
AWM 3	−2[c]	(E+S0)/Sp ≈ 1[c]	I[g] or II[c]	NGC 5629	≤2[o]
MKW 4	−1[c]	(E+S0)/Sp ≈ 1[c]	I[c,h]	NGC 4073	4 ± 4[o]

[a] Sandage & Hardy 1973.
[b] Leir & van den Bergh 1977.
[c] Bahcall 1980.
[d] Ferguson & Sandage 1988.
[e] Melnick & Sargent 1977.
[f] Oemler 1974.
[g] Albert et al. 1977.
[h] Morgan et al. 1975.
[i] Bridges et al. 1991.
[j] Harris et al. 1983.
[k] Butterworth & Harris 1992.
[l] Harris 1987; Thompson & Valdes 1987.
[m] Harris et al. 1993.
[n] Pritchet & Harris 1990.
[o] Bridges & Hanes 1993.

Morgan (1970) type of each cluster. Here we see (neglecting for a moment UGC 9958 in A 2107) that there is better correspondence between S_N and this property of the cluster: those clusters of Bautz-Morgan class I or I–II have centrally dominant galaxies with *low* S_N ($\lesssim 5$), while the high-S_N GCSs are found in clusters of type II or III.[2] The significance of this result is that BM class I and I–II clusters are generally in a more advanced stage of dynamical evolution than their type II, II–III, and III counterparts (Sandage & Hardy 1973; Oemler 1974; Bahcall 1977; Leir & van den Bergh 1977; Hausman & Ostriker 1978). Since it seems reasonable to expect mergers to play a part in this dynamical evolution, we might then postulate that all or most centrally dominant galaxies do indeed somehow *form* GCSs with high S_N, but that as time goes by the globular cluster populations of these galaxies can be diluted by (gas-poor) mergers with lower S_N systems (Harris 1981), so the most evolved clusters have central galaxies with only average, or even below average, S_N. In this context, the exception of UGC 9958 (i.e., a high-S_N galaxy in a BM type I cluster) may be explained by noting that Oegerle & Hill 1992) have found this galaxy to have a moderately high peculiar velocity of some 270 km s^{-1} with respect to the cluster mean, which indicates that this cluster is perhaps not as highly evolved as its BM classification would suggest.

The sample in Table 14, though small, indicates to us that high-S_N GCSs must have this feature built in essentially at birth; subsequent evolution in a cluster environment seems incapable of producing a high S_N in and of itself, and more likely has the opposite net effect. An interesting sidelight on this point is provided by the case of NGC 6166: since its parent cluster (A 2199) is of BM type I, it is presumably in an advanced evolutionary state and may even have undergone collapse (Oemler 1974); if this is so, and if the collapse leads both to an enhanced merger rate in the cluster core and to the shredding of large, weakly bound protospirals there (with the gas being returned to the intracluster medium; Whitmore et al. 1993), then we can qualitatively explain both the relatively high luminosity of this galaxy's X-ray halo and the relatively low specific frequency of its GCS (as compared to M87).

These ideas permit a final comment on Table 13. As is evident from the table, and derived in MHH, the cD envelope of M87 ($R \geq 4'.5$) has roughly the same high specific frequency as the main body of the galaxy. Further, the structural similarity of the halo light and the GCS in the envelope of M87 (the excesses of flux and of globular clusters both begin sharply at $R \simeq 4'.5$, and respectively represent $\sim 10\%$ of the total luminosity and GCS population of the galaxy) suggests that these two components share a common origin. The possible origins of cD envelopes (Dressler 1984, and references therein) include one or more of the following: collisional stripping in virialized clusters, star formation in cooling flows, cannibalism and mergers, and tidal stripping during cluster collapse (primordial origin). MHH argue that the high S_N is an indication that the globulars in the cD envelope (as well as in the main body of the galaxy) must have formed in situ rather than being brought in from elsewhere, because no other Virgo galaxies have $S_N \gtrsim 20$.[3] Further support of this conclusion comes from the fact that both the GCLF (§ 5.2) and the GCS metallicity distribution function (Lee & Geisler 1993) are the same in the cD envelope as in the rest of the galaxy, and from the observation that the major axis of the envelope GCS coincides with that of the halo light (§ 4). We therefore regard as unlikely the possibility that the corona of the M87 GCS (and hence the entire cD envelope) could have formed by the collisional stripping of Virgo galaxies after star formation was finished. If the cD envelopes of other high-S_N galaxies are found to have the same high-S_N excess GCS component, then we can probably discount this mechanism altogether as a way to cD envelope formation (at least in BM type type II and III clusters).

The cooling flow mechanism is consistent with the in situ formation of globulars in the cD envelope. As mentioned above, though, it is probably not responsible for the high specific frequency there. But if cooling flows cannot explain the envelope of the GCS, then by hypothesis they cannot explain the cD envelope at all; thus we reject this possibility as well.

Cannibalism and *stellar* mergers (as opposed to gaseous mergers, which are perhaps more properly considered as "primordial" processes), as a source of energy which distends the outer regions of M87, would be consistent with the requirement that the high specific frequency of the GCS be present from the outset. Note, though, that a large number of mergers among roughly equal-size progenitors may tend to put material in an envelope around the resulting galaxy, but could significantly lower the specific frequency of the GCS (Harris 1981). Furthermore, there is no indcation that M87 has suffered a greater number of mergers than any typical giant elliptical (Malumuth & Kirshner 1981); and if it had, it would be difficult to explain the observed color gradients in the GCS (Strom et al. 1981; Lee & Geisler 1993). Therefore, we look to cannibalism (i.e., the swallowing of galaxies which are so small as to have a negligible effect on the specific frequency of the system as a whole), rather than mergers per se, to produce the observations. However, the N-body experiments of Duncan, Farouoki, & Shapiro (1983) show that this process has a much greater effect on the inner bodies of cDs than on their outer regions; typically, the luminosities of the envelopes formed in these simulations are only $\sim 10\%$ of the luminosity of the underlying galaxy. While this is just the right order of magnitude to explain the M87 corona, it is *not* a large enough effect to account for the huge scale lengths and luminosities of cD envelopes in general (Schombert 1988). *If* it can be said that a single mechanism is responsible for the formation of all cD envelopes, then it would seem that the envelope of M87 is not

[2] An obvious difficulty here is the subjective nature of the BM classification scheme (e.g., Leir & van den Bergh 1977). For example, Abell, Corwin, & Olowin (1989) list A 2052 as BM type I–II (as opposed to the class II assignment quoted in Table 14), and Fornax (designated Abell S0373) as type I rather than II–III. (The BM types of all the other clusters in our list are unchanged in this newer catalog.) However, Bautz & Morgan (1970) state that A 2052 is a type II cluster on the basis of relative luminosity, and type I–II on the basis of relative *size*. The Fornax discrepancy is more dramatic; but since, for example, the cluster elliptical NGC 1404 is only 0.4 mag fainter than the brightest core galaxy, NGC 1399, we have gone with the classification given in Table 14 for this cluster. It should also be noted that the Bautz-Morgan scheme was originally intended to be applied to rich clusters; its meaning for poorer clusters, like AWM 3 or MKW 4, is not clear.

[3] Inspection of Fig. 21 shows that for a more normal Virgo elliptical such as M49, S_N can in fact reach these values at $R \gtrsim 15'$, which corresponds to $\gtrsim 65$ kpc for a Virgo distance of 15 Mpc. It might be said, then, that collisional stripping could indeed take high-S_N portions of GCSs from the outskirts of other Virgo members and deposit them on M87 at a radius where there is *coincidentally* roughly the same mix of globulars and halo field stars. However, the vast spatial extent of the M49 GCS, like its M87 counterpart, is certainly atypical of normal-size ellipticals, and it thus seems unlikely that enough globulars could be taken from such outer regions to produce the observed effect; moreover, it would indeed be a great stroke of luck to have the stripped material deposited at just the right place in M87 to give the same S_N for the envelope and the main body of the galaxy.

the consequence of merging or cannibalism after star formation. This conclusion would be strengthened by the detection of high S_N in more extreme cD envelopes (e.g., that of NGC 1399 in Fornax) whose origins could in no way be attributed to late mergers; but the possibility remains that the M87 corona formed through cannibalism, while other cD envelopes did not.

We are left then with the primordial origin hypothesis, in which collisional stripping and dynamical friction due to the intracluster medium (which could lead to mergers with a central galaxy) are rather inefficient in relaxed clusters, so that it is difficult to form either the body or the envelope of a cD *after* cluster virialization (Merritt 1984, 1985). In addition, the observational evidence appears to favor the idea that cD envelopes are "structurally, dynamically, and compositionally distinct" from the main bodies of their parent galaxies (Mackie 1992); thus these structures may consist, at least partly and perhaps even wholly, of material accreted early in the life of a cluster (i.e., before or during cluster collapse, or during evolution in subclumps which later merge to form a cluster). In the case of M87 specifically, the *sharpness* of the break in the galaxy's surface brightness and GCS profiles at $R = 4'.5$ is consistent with the interpretation that its envelope was added on to some already well-defined parent body. If we are to mesh this conclusion with our M87 GCS data, it seems most logical to demand that the cD envelope of this galaxy be accreted while still mostly gaseous.

The pair of galaxies NGC 1399 and NGC 1404 in the Fornax cluster may provide an interesting test of this hypothesis. NGC 1399 is a central cD with high S_N, while NGC 1404 is a more normal large elliptical, but with an abnormally *low* S_N ($\simeq 1$–2; Hanes & Harris 1986b; Richtler et al. 1992). These galaxies are only separated by $\simeq 10'$ on the sky, so particularly large quantities of gas may have been stripped from NGC 1404 very early on, later to form part of the cD envelope of NGC 1399. Such a process could conceivably inhibit (or even truncate) the formation of globular clusters in NGC 1404 and might thus explain its markedly subnormal specific frequency (but see Richtler et al. 1992 for an alternative explanation of the properties of this galaxy). Again, the detection of a high specific frequency for the cD envelope of NGC 1399 would support the idea that it was accreted while gaseous.

7. SUMMARY

The advent of large format CCDs is permitting us to learn anew about the character of GCSs on large scales. Four principal results have emerged from the present study.

First, as MHH also detailed, an envelope-like component of the M87 GCS, accounting for $\sim 10\%$ of the galaxy's total globular cluster population, has been detected at $R \geq 4'.5$. The size and location of this feature indicate that it is part of the cD envelope of M87, and its high specific frequency has proven to be an interesting discriminator between various ideas on cD envelope formation. In particular, our observations are most consistent with a scenario in which the envelope of M87 is collected around the main body of the galaxy while still in a gaseous state. In turn, such a scenario is most similar to Merritt's (1984) idea of a "primordial origin" for these structures.

Second, we have shown that the M87 GCS is significantly flattened, with a position angle which roughly matches that of the galaxy itself, but with a steeper ellipticity gradient inside $R = 4'.5$. This last point remains unexplained, but may be a reflection of the relation between the GCS and the dark matter halo of M87, and/or of the preferential destruction of globulars on box orbits in the core of the system.

Third, we have extended to larger radii the result that the bright half of the M87 GCLF shows no variation with galactocentric distance; the Gaussian which best describes the GCLF has $\sigma \simeq 1.7$ and $V^0 \simeq 24.2$ over the entire range $0'.5 \lesssim R \lesssim 7'$.

Finally, the most outstanding problem in GCS research—the high-S_N phenomenon—continues to deserve a good deal of attention. The evidence to date is that this phenomenon shows itself almost exclusively in the central galaxies of Bautz-Morgan class II or III clusters. If we accept the idea that the BM sequence is primarily an evolutionary one, and recall the lack of any observed correlation between central galaxies' S_N and their parent clusters' global properties (richness, galaxy content, X-ray luminosity), then the suggestion is that a high S_N is the result of local initial conditions during galaxy formation. The challenge is to understand just what these conditions are, and precisely how they lead to a huge overproduction of globular clusters.

We are grateful to Ray Carlberg and Scott Tremaine for helpful comments. D. E. M. would also like to thank Phil Fischer for his assistance in the early stages of this project. This work was supported by the Natural Sciences and Engineering Research Council of Canada, through operating grants to W. E. H. and D. A. H. and a graduate fellowship to D. E. M.

REFERENCES

Abell, G. O. 1958, ApJS, 3, 211
Abell, G. O., Corwin, H. G., & Olowin, R. P. 1989, ApJS, 70, 1
Aguilar, L., Hut, P., & Ostriker, J. P. 1988, ApJ, 335, 720
Albert, C. E., White, R. A., & Morgan, W. W. 1977, ApJ, 211, 309
Ashman, K. M., & Zepf, S. E. 1992, ApJ, 384, 50
Bahcall, N. A. 1977, ARA&A, 15, 505
———. 1980, ApJ, 238, L117
Baum, W. A. 1955, PASP, 67, 328
Bautz, L. P., & Morgan, W. W. 1970, ApJ, 162, L149
Bolte, M. 1989, ApJ, 341, 168
Breiman, L. 1968, Probability (Reading, MA: Addison-Wesley)
Bridges, T. J., & Hanes, D. A. 1992, AJ, 103, 800
———. 1993, in The Globular Cluster—Galaxy Connection, ed. G. Smith & J. Brodie, (ASP Conf. Ser. 48), 544
Bridges, T. J., Hanes, D. A., & Harris, W. E. 1991, AJ, 101, 469
Buote, D. A., & Canizares, C. R. 1992, ApJ, 400, 385
Burstein, D., & Heiles, C. 1984, ApJS, 54, 33
Butterworth, S. T. 1991, M.Sc. thesis, McMaster Univ.
Butterworth, S. T., & Harris, W. E. 1992, AJ, 103, 1828
Carter, D., & Dixon, K. L. 1978, AJ, 83, 6
Carter, D., & Metcalfe, N. 1980, MNRAS, 191, 325
Cohen, J. G. 1986, AJ, 92, 1039
———. 1988, AJ, 95, 682
Couture, J., Harris, W. E., & Allwright, J. W. B. 1990, ApJS, 73, 671
de Vaucouleurs, G., & Nieto, J.-L. 1978, ApJ, 220, 449 (dVN)
Dressler, A. 1980, ApJ, 236, 351
———. 1984, ARA&A, 22, 185
Dubinski, J., & Carlberg, R. G. 1991, ApJ, 378, 496
Duncan, M. J., Farouki, R. T., & Shapiro, S. L. 1983, ApJ, 271, 22
Fabian, A., Nulsen, P., & Canizares, C. 1984, Nature, 310, 733
Ferguson, H. C., & Sandage, A. 1988, AJ, 96, 1520
Fischer, P., Hesser, J. E., Harris, H. C., & Bothun, G. D. 1990, PASP, 102, 5
Forte, J. C., Martinez, R. E., & Muzzio, J. C. 1982, AJ, 87, 1465
Forte, J. C., Strom, S. E., & Strom, K. M. 1981, ApJ, 245, L9
Franx, M., Illingworth, G., & de Zeeuw, T. 1991, ApJ, 383, 112
Grillmair, C., Pritchet, C., & van den Bergh, S. 1986, AJ, 91, 1328
Hanes, D. A. 1971, M.Sc. thesis, Univ. Toronto
———. 1977a, MNRAS, 179, 331
———. 1977b, MNRAS, 180, 309
Hanes, D. A., & Harris, W. E. 1986a, ApJ, 304, 599

Hanes, D. A., & Harris, W. E. 1986b, ApJ, 309, 564
Hanes, D. A., & Whittaker, D. G. 1987, AJ, 94, 906
Harris, W. E. 1981, ApJ, 251, 497
———. 1986, AJ, 91, 822
———. 1987, ApJ, 315, L29
———. 1990, PASP, 162, 966
———. 1991, ARA&A, 29, 543
Harris, W. E., & Racine, R. 1979, ARA&A, 17, 241
Harris, W. E., & Smith, M. G. 1976, ApJ, 207, 1036
Harris, W. E., & van den Bergh, S. 1981, AJ, 86, 1627
Harris, W. E., Harris, H. C., & Harris, G. L. H. 1984, AJ, 89, 216
Harris, W. E., Smith, M. G., & Myra, E. S. 1983, ApJ, 272, 456
Harris, W. E., Pritchet, C. J., & McClure, R. D. 1993, in The Globular Cluster–Galaxy Connection, ed. G. Smith & J. Brodie, (ASP Conf. Ser. 48), 572
Harris, W. E., Allwright, J. W. B., Pritchet, C. J., & van den Bergh, S. 1991, ApJS, 76, 115
Hausman, M. A., & Ostriker, J. P. 1978, ApJ, 224, 320
Jacoby, G. H., et al. 1992, PASP, 104, 599
King, I. R. 1978, ApJ, 222, 1
Kormendy, J. 1988, ApJ, 335, 40
Kron, R. G. 1980, ApJS, 43, 305
Kumai, Y., Basu, B., & Fujimoto, M. 1993, ApJ, 404, 144
Lauer, T. R., & Kormendy, J. 1986, ApJ, 303, L1
Lauer, T. R., et al. 1992, AJ, 103, 703
Lee, M. G., & Geisler, D. 1993, AJ, 106, 493
Leir, A. A., & van den Bergh, S. 1977, ApJS, 34, 381
Liller, M. H. 1960, ApJ, 132, 306
Mackie, G. 1992, ApJ, 400, 65
Malumuth, E. M., & Kirshner, R. P. 1981, ApJ, 251, 508
Malumuth, E. M., & Richstone, D. O. 1984, ApJ, 276, 413
McLaughlin, D. E., Harris, W. E., & Hanes, D. A. 1993, ApJ, 409, L45 (MHH)
McMillan, S. L. W., Kowalski, M. P., & Ulmer, M. P. 1989, ApJS, 70, 723
Melnick, J., & Sargent, W. L. W. 1977, ApJ, 215, 401
Merritt, D. 1984, ApJ, 276, 26
———. 1985, ApJ, 289, 18
Morgan, W. W., Kayser, S., & White, R. A. 1975, ApJ, 199, 545
Oegerle, W. R., & Hill, J. M. 1992, AJ, 104, 2078
Oemler, A. 1974, ApJ, 194, 1
Ostriker, J. P., Binney, J., & Saha, P. 1989, MNRAS, 241, 849
Press, W. H., Teukolsky, S. A. Vetterling, W. T., & Flannery, B. P. 1992, Numerical Recipes in Fortran (2d ed.; Cambridge: Cambridge Univ. Press)
Pritchet, C. J., & Harris, W. E. 1990, ApJ, 355, 410
Racine, R. 1968a, JRASC, 62, 367
———. 1968b, PASP, 80, 326
Richtler, T., Grebel, E. K., Domgorgen, H., Hilker, M., & Kissler, M. 1992, A&A, 264, 25
Ryden, B. S. 1992, ApJ, 396, 445
Sandage, A., & Hardy, E. 1973, ApJ, 183, 743
Schombert, J. M. 1988, ApJ, 328, 475
Secker, J. 1992, AJ, 104, 1472
Secker, J., & Harris, W. E. 1993, AJ, 105, 1358
Stetson, P. B. 1987, PASP, 99, 191
Strom, S. E., Forte, J. C., Harris, W. E., Strom, K. S., Wells, D. C., & Smith, M. G. 1981, ApJ, 245, 416
Thompson, L. A., & Valdes, F. 1987, ApJ, 315, L35
Trumpler, R. J., & Weaver, H. F. 1953, Statistical Astronomy (New York: Dover)
van den Bergh, S. 1984, PASP, 96, 329
van den Bergh, S., Pritchet, C., & Grillmair, C. 1985, AJ, 90, 595
Whitmore, B. C., Gilmore, D. M., & Jones, C. 1993, ApJ, 407, 489